

國立交通大學

電機學院

光電工程研究所

碩士論文

從物理系統之自發擾動行為探討其低激發態特性

**Probing Low-Level Excitation Properties of Physical Systems
from Their Spontaneous Fluctuation Behaviors**

研究生：陳秉寬

指導教授：黃中堯

中華民國九十七年四月

從物理系統之自發擾動行為探討其低激發態特性

**Probing Low-Level Excitation Properties of Physical Systems
from Their Spontaneous Fluctuation Behaviors**

研究生：陳秉寬

Student : Bing-Kuan Chen

指導教授：黃中堯

Advisor : Jung Y. Huang

國立交通大學
光電工程研究所
碩士論文

A Thesis Submitted to
Institute of Electro-Optical Engineering
College of Electrical Engineering and Computer Science
National Chiao Tung University
in Partial Fulfillment of the Requirements
for the Degree of
Master
in
Electro-Optical Engineering

April 2008
Hsinchu, Taiwan, Republic of China

從物理系統之自發擾動行為探討其低激發態特性

研究生:陳秉寬

指導教授:黃中堯

國立交通大學光電工程研究所

摘要

古典統計力學的擾動耗散定理闡明了「低維激發態所引起的自發擾動行為存在所有凝態物理系統中」,本論文之研究主旨即在探討特定凝態材料-液晶的分子動態擾動現象。

液晶分子與液晶盒基板間的錨定作用力大小與表面配向處理的方法有關。本論文由動態光散射理論出發,輔以液晶指向矢流體動力方程式與特定邊界條件,推得經液晶散射之光訊號其特徵相關時間與錨定能係數間之關係式,並以實際合成不同表面配向處理的向列型液晶盒為實驗樣本,由動態光散射實驗得到符合理論預測之結果,即液晶顯示器工業常使用的摩擦配向法所造成的錨定作用力,大於光配向法所造成的錨定作用力,其錨定能係數相差約兩個數量級;並且,於配向層上沉積液晶聚合物確能有效提升液晶分子排列品質。

表面穩定型鐵電相液晶元件具有高應答速度、寬視角範圍等優點,然鐵電相結構因不易完美排列而產生缺陷的缺點,限制了其在工業應用方面的發展。參雜氧化鋅奈米晶體的表面穩定型鐵電相液晶元件由於奈米晶體引致的分子束縛效應有效地提升了鐵電相液晶分子的排列品質;本論文觀察到因排列品質的提升使得部份鐵電相液晶分子脫離表面錨定作用力影響的現象。

Probing Low-Level Excitation Properties of Physical Systems from Their Spontaneous Fluctuation Behaviors

Student: Bing-Kuan Chen

Advisors: Jung Y. Huang

**Institute of Electro-Optical Engineering,
National Chiao Tung University**

Abstract

The fluctuation-dissipation theorem of classical statistical mechanics reveals that there always exist spontaneous fluctuation behaviors induced by low-level excitations in all condensed matter physical systems. The main theme of this thesis study lay in the discussion about the dynamical molecular fluctuations of specific condensed matter material – liquid crystal (LC).

The anchoring strength of a LC cell is relevant to the surface treatment methods. In this thesis, we began the derivations from the dynamic light scattering theory, together with the hydrodynamic equation of LC director and certain specific boundary conditions. We finally obtained the relationship between the correlation time of the scattering light scattered by LC and the anchoring energy coefficient of the cell. After measuring the scattering light coming from various nematic cells with different surface treatments, the results obtained from dynamic light scattering technique confirmed the theoretical predictions well, that is, the anchoring energy coefficient produced by mechanical rubbing method that is often used in liquid crystal display industry is larger than that produced by photoalignment method by around two order of magnitude; moreover, depositing liquid crystal polymer on the photoalignment layer of the cell does improve the LC alignment quality.

Surface-stabilized ferroelectric liquid crystal devices have merits of fast response speed and wide viewing angle. However, the tendency toward defect formation owing to imperfect molecular alignment restrains their development in industrial applications. Doping ZnO nanocrystals into ferroelectric liquid crystal host can improve the quality of liquid crystal molecular alignment by virtue of the molecular binding effect. In this thesis, we observed a novel phenomenon that a portion of the liquid crystal molecules got rid of the influence of surface anchoring because of the improvement of doping-induced orientational order.

Acknowledgement

記得第一次處理實驗數據，自己天真地寫了一組 loops 去跑 bk-style data fitting，興沖沖地把結果拿去與指導教授 黃中堯 博士討論，沒料到這種 data fitting 方式是完全不被科學界所認可的，黃老師嚴肅地提出了糾正：「沒人這樣搞的!!!」，這一幕，發生在黃老師於交映樓的系主任辦公室裡，迄今仍深烙在我腦海。從那時起，我深深體會到自己離所謂的「作研究」尚有一段十分遙遠的距離。對於科學研究，我曾經無知到令人搖頭，感謝黃老師，對一個什麼都不懂的傢伙，展現出如此寬大的包容，花了不少寶貴的時間引領我走向正途。“絕不輕易說做不到”的研究態度，是黃老師給我的最大啟發，無數次的失敗實驗造就了堅毅的心理素質，而這正是科學研究要成功的條件之一，雖不充分，卻是必要。

感謝 謝文峰 教授、黃衍介 教授與 李瑞光 教授，在我碩士論文口試中提供了不少寶貴的意見。並且，您們在我碩士生涯最後所譜下的精采攻防，將成為我永生難忘的美好回憶。

Thank Dr. *Brogioli* for providing me with some practical suggestions about light scattering experiment and some useful background knowledge about various types of optoelectronic instruments. I deeply appreciate your kindly help.

在研究中遇到挫折時，感謝 桂珠 學姊總是以過來人的經驗給予我心靈上的撫慰。感謝 旭政 學長熱心的鼓勵並強烈地建議我到黃老師實驗室接受最嚴謹的科學訓練。謝謝非線性光學實驗室的每位成員：柳萱、雲漢、建輝、綿綿、燦丞、建佑 和 *Bastein*，有你們的陪伴，使得每個不太像週末的週末多了幾分活潑的氣息；還有光電教學實驗室的 明頤，在工業電子相關知識方面提供了不少幫助。

最後，也是最重要的，我要誠摯地感謝我的家人，您們的存在在我內心深處已是一股穩定力量的來源，縱使沒有話語形式的表達。尤其感謝的是我的父母，沒有您們精神上與物質上的支持，就不可能有今日的我，謹以此碩士論文獻給您們二位。

Table of Contents

Abstract (in Chinese)	i
Abstract (in English)	ii
Acknowledgement	iii
Table of Contents	iv
List of Figures	vi
List of Tables	xi

Chapter 1 Introduction	1
1.1 Fluctuation and Dissipation Theorem of a Physical System.....	1
1.1.1 Langevin Equation for Brownian Motion.....	2
1.1.2 Stochastic Process.....	4
1.1.3 Derivation of the Fluctuation-Dissipation Theorem (FDT) of a Physical System.....	8
1.2 Light Scattering from a Physical System.....	11
1.2.1 Basic Concepts of Light Scattering.....	11
1.2.2 Electromagnetic Theory of Light Scattering.....	14
1.3 Autocorrelation Function of Scattered Photons from a Physical System....	19
1.3.1 Basic Concepts of Autocorrelation Function.....	19
1.3.2 Implementation of Autocorrelation Function.....	24
1.3.3 Test Run of Flex02-01D Digital Correlator.....	28

Chapter 2 Probing the Twist Anchoring Strength of Liquid Crystal Molecules on

Various Alignment Surfaces.....	41
2.1 Overview of Liquid Crystals Phases.....	41
2.2 Theoretical Background of Molecular Fluctuations in Liquid Crystals.....	43
2.2.1 Broken Symmetry and Elementary Excitations.....	43
2.2.2 Orientational Fluctuations in Thin Nematic Liquid Crystal Cells...	47
2.3 The Relationship of the Anchoring Energy Strength with Autocorrelation Time and Its Measurement with Dynamic Light Scattering.....	53
2.4 The Twist Anchoring Strength of Nematic Liquid Crystal Molecules on Various Alignment Surfaces.....	57
2.4.1 Experimental Setup and Considerations.....	59
2.4.2 Experimental Results and Discussion.....	62
Chapter 3 Probing the Thermal Fluctuation in the Conic Motion of Surface Stab- ilized Ferroelectric Liquid Crystals.....	72
3.1 Introduction to the Physics of SSFLC.....	72
3.1.1 Basic Concepts of Ferroelectric Liquid Crystals.....	72
3.1.2 Optical Properties of SSFLC.....	76
3.2 Experimental Study of the Dynamic Light Scattering from Pure SSFLC and Nanocrystalline–ZnO Doped SSFLC.....	78
3.2.1 Experimental Setup.....	79
3.2.2 Experimental Results and Discussion.....	81
Chapter 4 Conclusions.....	95
References.....	97

List of Figures

Fig. 1-2-1 The total radiated field observed at Detector is the superposition of those radiated from all infinitesimal elements d^3r' at positions \vec{r}' with respect to the center of the illuminated volume.....17

Fig. 1-3-1 Typical noise-like pattern of a physical property Y . The time axis is divided into discrete intervals, Δt in width, and $\langle Y \rangle$ means the time average of Y 21

Fig. 1-3-2 Computation of the photoelectron-count autocorrelation function at stage $\tau_2 = 2T$. $n(t_i)$, denoted by $n(i)$, is the number of photocounts detected at time t_i over a sampling time T . In this case,

$$M(2T) = \left(\frac{1}{N-2}\right) \sum_{i=1}^{N-2} n(t_i)n(t_{i+2}) = \left(\frac{1}{N-2}\right)(6+0+8+\dots) \dots\dots\dots 26$$

Fig. 1-3-3 Schematic illustration of Dynamic Light Scattering experiment and operation of the digital correlator. 1, 2, 3,..., L are delay-time indices with delay-time increment T 27

Fig. 1-3-4 (a) Incident plane waves (dotted lines) travel in the direction of \vec{k}_i . Spherical scattered wavefronts (dotted circles) from spheres are brought about. The detector will be placed in the direction of \vec{k}_f that is shown by interference of two particles' scattered spherical wave; O represents the reference sphere, and P represents another sphere located in \vec{r}_j relative to O ; **(b)** The scattering is quasi-elastic so that $|\vec{k}_i| = |\vec{k}_f|$ and $\vec{q} = 2|\vec{k}_i| \sin(\theta/2) \hat{q}$ 29

Fig. 1-3-5 Schematic experimental setup for determining particle size in the sample

solution. M:mirror ; P:polarizer ; L:lens ; D:diaphragm.....	35
Fig. 1-3-6 (a) The intensity (kilo-photocounts per second) trace recorded the scattering light intensity scattered from 100% (wt%) ethylene glycol solution in which 12-nm Au nanoparticles suspended; (b) the autocorrelation function calculated from the intensity information in (a)	37
Fig. 2-1-1 Spatial arrangements of elongated molecules in various phases. Smectic and nematic phases belong to liquid crystalline phase ; \hat{n} means their directors.....	43
Fig. 2-2-1 The comparison of positional order in solids crystals and orientational order in nematic liquid crystals; the bottom two figures are their corresponding dispersion relations. Note that they both show the presence of zero-frequency modes; \vec{q} is wavevector of fluctuation, \vec{n}_0 is the average orientation of the director, $\delta\vec{n}$ is the fluctuation of the director, τ is the relaxation time of $\delta\vec{n}$, $\omega(q)$ is the oscillating frequency of the phonons.....	45
Fig. 2-2-2 (a) coherent collective excitations in solid crystals; (b) coherent collective excitations in liquid crystals.....	47
Fig. 2-2-3 The three types of deformation in nematics. \hat{n} represents their director.....	48
Fig. 2-2-4 Definition of the new coordinates system in LC.....	50
Fig. 2-3-1 τ_c is the τ -position at which the two sections (blue & red) are equal in area; in the case of exponentially decaying fluctuation, τ_c is equal to its relaxation time τ_r	54
Fig. 2-4-1 Experimental setup for measuring the anchoring energy coefficients. M: mirror ; P_1 & P_2 : polarizers ; L: lens ; D: diaphragm ; the polarization of	

the incoming beam \hat{i} is parallel to the LC's director \hat{n} , but perpendicular to the outgoing beam's polarization \hat{f} and the scattering plane. The scattering angle was chosen small, 3° in this experiment, so as to minimize the contribution of splay / bend fluctuations.....59

Fig. 2-4-2 The scattering angle was so small that the scattering vector \vec{q} was almost parallel to the substrates, which made it possible to probe the pure twist component of the fluctuations.....60

Fig. 2-4-3 The colorful circle lines are the measured raw data, and the black solid lines are their corresponding fitting results. The fitting model is the stretched exponential function $g^{(2)}(t) = A + B \exp[-(t/\tau)^s]$. τ is the correlation time and s is the stretching parameter.....63

Fig. 2-4-4 The self-similarity existing in the collective excitation of LC *Goldstone* mode: Yellow wave represents the incident light field. $n(1)$ is the photoelectron pulses counted at initial time, and $n(\tau)$ is the photocounts at a delay τ from the initial time.....66

Fig. 2-4-5 (a) Effective λ_E of the collective excitation-induced standing wave in the strong anchoring cell; **(b)** effective λ_E of the collective excitation-induced standing wave in the weak anchoring cell.....69

Fig. 2-4-6 (a) The structural formula of the LCP used in our experiment; **(b)** the morphological change of the LCP in the *photopolymerization* process...70

Fig. 2-4-7 (a) Distribution of correlation times of the three cells with different surface treatments. 50 points were probed for each cell. The abscissa is correlation time and the ordinate is its corresponding population; **(b)** distribution of stretching parameters of the three cells with different

surface treatments. 50 points were probed for each cell. The abscissa is stretching parameter and the ordinate is its corresponding population....71

Fig. 3-1-1 (a) Smectic A phase; **(b)** smectic C phase, where θ is the tilt angle and \hat{n} is the director of the LC. **(c)** For thermotropic matter, different phase corresponds to different temperature range. The Smectic C phase exists in the lower temperature range than the smectic A phase does.....73

Fig. 3-1-2 The first ferroelectric liquid crystal molecule DOBAMBC. The carbon atom marked by an asterisk (*) is referred to as an asymmetric one. \vec{P} represents the spontaneous polarization of the molecule.....75

Fig. 3-1-3 The layered structure of SmC^* . The chiral molecule with specific spontaneous polarization rotates around the layer normal to outline a cone from layer to layer with a typical helical pitch of a few microns. The director \hat{n} makes the same angle θ with the layer normal. \vec{P} represents its induced electric polarization.....76

Fig. 3-1-4 Two bistable states of a bookshelf type SSFLC device. The polarity of the external applied electric field switches the device on either **(a)** dark state or **(b)** bright state.....77

Fig. 3-2-1 The scheme is similar to that shown in Fig. 2-4-1. H represents the heating stage. Note that \hat{n}_1 is the direction in one of the two orientational states, which is shown in Fig. 3-1-4. A function generator was used to switch the SSFLC cell between two bistable states.....80

Fig. 3-2-2 The autocorrelation functions of the scattered light signals correspond to externally sinusoidal driving voltages with different driving frequencies. The small hollow circles represent the measured raw data while the red lines represent the fitting curves.....81

Fig. 3-2-3 (a) The top figure shows the intensity trace collected in duration of 7,200

seconds for the undoped SSFLC cell while the bottom shows the corresponding autocorrelation function (hollow circle line) and its fitting curve (red line); **(b)** the case for the nc-ZnO-doped SSFLC cell. Note that in both intensity traces in **(a)** and **(b)**, they exhibit not only global fluctuation but also local fluctuation.....85

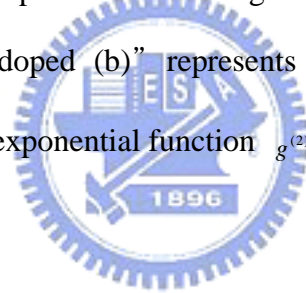
Fig. 3-2-4 In SmC^* , **(a)** $\vec{\xi}$ is the in-plane projection of the molecular tilt and \vec{P} is the spontaneous electric polarization on a plane parallel to $\hat{x} - \hat{y}$ plane. **(b)** the small fluctuations of the tilt and the polarization.....89

Fig. 3-2-5 The three fluctuation modes observed in the measurement. \vec{q} represents the scattering vector.....93

Fig. 3-2-6 In the upper figure, the left two circles represent the orbits traversed by the ends of the FLC molecules. One of them is in the unaffected region while the other one is in the balanced region; the left figure show the conic motion of the LC molecules in the balanced region.....93

List of Tables

Table 1-3-1 The 12 nm nanoparticle’s hydrodynamic diameters correspond to various viscous solutions; E.G. wt% means ethylene glycol’s percentage of the water solvent; n represents index of refraction; η represents viscosity of solution; τ_c represents characteristic decay time of the autocorrelation function.....	39
Table 3-2-1 The fitting results of Fig. 3-2-2. Note that the parameters ω and p are correlated.....	82
Table 3-2-2 The fitting results of the two autocorrelation functions in Fig. 3-2-3. Here, “undoped (a)” represents the fitting results by using the fitting model Eq. (3.2.2); “undoped (b)” represents the fitting results by using a double stretched exponential function $g^{(2)}(t) = A + C \cdot e^{-(t/\tau_2)^2} + D \cdot e^{-(t/\tau_3)^3}$	88



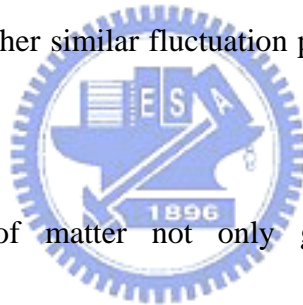
Chapter 1. Introduction

1.1 Fluctuation and Dissipation Theorem of a Physical System

When a physical system is in thermal equilibrium, its thermodynamic quantities shall be constant. However, if one could measure those quantities precisely and rapidly, he or she will find that the measured values undergo small fluctuations [1].

For example, the pressure on a surface of an object immersed in a medium (such as air, water, *etc.*) changes rapidly. These small fluctuations come from the irregular impact

of molecules. So is true for other similar fluctuation phenomena, which comprise the granular nature of matter.



The granular nature of matter not only gives rise to fluctuations of thermodynamic quantities, it also explains why there exists friction (the reason for the dissipation of energy). To illustrate the essential idea indispensable for this thesis

study, let us begin a discussion about the fluctuation phenomenon of a physical system with a Brownian motion of colloidal particles suspending in a liquid medium.

In the following, we will derive the relation between fluctuation and dissipation of this physical system through a mathematically descriptive model known as *Langevin* equation.

1.1.1 Langevin Equation for Brownian Motion

Considering a group of sufficiently small particles immersed in a liquid medium, the particles exhibit an irregular motion. This type of motion is called “Brownian motion” in honor of Scottish naturalist **Robert Brown** (1773–1858), who investigated the phenomenon in 1827 [2]. The system yields a direct insight into the mechanism responsible for the existence of fluctuations, dissipation of energy, and the relationship between them.

To simplify our description, we shall treat this problem in one-dimensional case.

Consider that a particle of mass m is immersed in a liquid medium at temperature T , and its center-of-mass position at time t is designated by $x(t)$ and the corresponding velocity is therefore $v \equiv dx/dt$. This particle’s dynamic behavior is governed by **Newton**’s second law of motion

$$m \frac{dv}{dt} = F_{ext}(t) + F(t), \quad (1.1.1)$$

where F_{ext} is an external force exerted by some external systems, such as gravity or electromagnetic fields; $F(t)$ denotes an effective interaction from many degrees of freedom (*i.e.*, such as those representing the atomic motion in the suspending particles or molecular motion in the surrounding medium) of the system. Apparently, $F(t)$ must be some rapidly fluctuating function of time t since it depends on the positions of many atoms which are in constant motion [3]. This makes $F(t)$ fluctuating in a

highly irregular fashion. Therefore, we cannot specify the exact dependence of $F(t)$ on t ; we must appeal to statistical language.

To begin with, we define the ensemble average of $F(t)$ to be an averaged value at time t over all the N subsystems, which is $\bar{F}(t) \equiv \frac{1}{N} \sum_{j=1}^N F_j(t)$.

Accordingly, we shall write

$$F = \bar{F} + \tilde{F} , \quad (1.1.2)$$

where \tilde{F} is the rapidly fluctuating part of F with its average $\langle \tilde{F} \rangle$ being zero.

Because of the existence of this fluctuating term, it follows from Eq. (1.1.1) that

velocity v also fluctuates in time. Hence, v is also able to be decomposed into an ensemble average \bar{v} and a fluctuating part \tilde{v} , $v = \bar{v} + \tilde{v}$. By the same token, \tilde{v} has zero mean just as \tilde{F} does. Intuitively, \bar{F} must be some function of \bar{v} such that

$\bar{F}(\bar{v}) = 0$ in equilibrium when \bar{v} equals zero. Under the condition that \bar{v} is not large, $\bar{F}(\bar{v})$ can be expanded in a power series of \bar{v} with the first nonvanishing term being linearly proportional to \bar{v} , which gives

$$\bar{F} = -\gamma \bar{v} = -\gamma(v - \tilde{v}) \approx -\gamma v , \quad (1.1.3)$$

where γ is a positive constant called “friction constant”, meanwhile, we have put

$\gamma \bar{v} \approx \gamma v$ since $\gamma \tilde{v}$ is negligibly small compared with the fluctuating \tilde{F} . Finally,

combining Eqs. (1.1.1), (1.1.2), and (1.1.3) leads to the “*Langevin* equation” for

Brownian motion,

$$m \frac{dv}{dt} = F_{ext} - \gamma v + \tilde{F}(t) . \quad (1.1.4)$$

We shall discuss the solution of this equation in the later context.

1.1.2 Stochastic Process

By definition, a deterministic variable must be exactly determined by given physical conditions. A random variable, on the contrary, is conceptually different from a deterministic variable. It can not possess a deterministic value. If one wants to describe a random variable's behavior, he or she must draw support from the statistical description. If some physical quantity X evolves with time t , we refer to this function $X(t)$ as a process. A physical process with random variables involved is called a "stochastic process". A *continuous memoryless* stochastic process is called a continuous **Markov** process. The term "continuous" means that $X(t+dt) \rightarrow X(t)$ as $dt \rightarrow 0$, and the term "memoryless" means that the process does not depend on any of its earlier values explicitly to advance itself from time t to time $t+dt$. In theory of statistics, a continuous **Markov** process guarantees that the increment $X(t+dt) - X(t)$ must have the analytical form of $A(X(t),t)dt + \sqrt{D(X(t),t)}N(t)\sqrt{dt}$. Here $A(X(t),t)$ and $D(X(t),t)$ can be any smooth function with $D(X(t),t)$ non-negative, $N(t)$ denotes an uncorrelated unit normal random variable, that is, $N(t)$ is a random variable with its mean value equal

to 0 and variance equal to 1. $N(t)$ is statistically independent of $N(t')$ when $t \neq t'$. From the above, we obtain

$$X(t+dt) = X(t) + A(X(t), t)dt + \sqrt{D(X(t), t)}N(t)\sqrt{dt} . \quad (1.1.5)$$

This equation is called the standard form of **Langevin** equation for the process X .

The function $A(X(t), t)$ in Eq. (1.1.5) is called the *drift function* of the process, and

$D(X(t), t)$ is called the *diffusion function* [4]. Rearranging Eq. (1.1.5) yields the

differential form

$$\frac{X(t+dt) - X(t)}{dt} = A(X(t), t) + \frac{\sqrt{D(X(t), t)}N(t)}{\sqrt{dt}} . \quad (1.1.6)$$

In order to solve such an equation, it is necessary to understand some basic properties about normal random variables. The normal random variable $N(m, \sigma^2)$ is

characterized by the probability density $p(x) = \frac{1}{\sqrt{2\pi\sigma^2}} \exp\left(-\frac{(x-m)^2}{2\sigma^2}\right)$,

$-\infty < x < \infty$, where the parameters m and σ^2 stand for the mean and variance

of N , respectively. Two essential properties of normal random variables arise:

$$\beta N(m, \sigma^2) = N(\beta m, \beta^2 \sigma^2) , \quad (1.1.7a)$$

$$N(m_1, \sigma_1^2) + N(m_2, \sigma_2^2) = N(m_1 + m_2, \sigma_1^2 + \sigma_2^2) . \quad (1.1.7b)$$

Then, if we define the Gaussian white noise process $\Gamma(t)$ as $\Gamma(t) \equiv \lim_{dt \rightarrow 0} N(0, \frac{1}{dt})$

and take the $dt \rightarrow 0$ limit in Eq. (1.1.6), we obtain

$$\frac{dX(t)}{dt} = A(X(t), t) + \sqrt{D(X(t), t)} \Gamma(t) . \quad (1.1.8)$$

This is the white noise form of *Langevin* equation [4]. There are also two properties of Gaussian white noise, which will be useful in the latter formulae derivation:

$$\langle \Gamma(t) \rangle = \mathbf{0} \quad (1.1.9a)$$

$$\langle \Gamma(t)\Gamma(t+t') \rangle = \delta(t') \quad (1.1.9b)$$

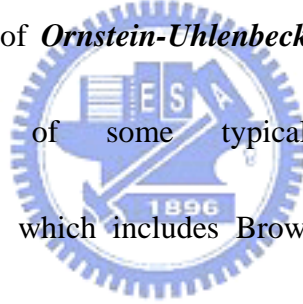
The angle bracket is the notation of taking average.

A continuous *Markov* process having the forms

$$A(X(t),t) = -\frac{1}{\tau}X(t) \quad , \quad D(X(t),t) = c \quad (1.1.10)$$

is called an *Ornstein-Uhlenbeck* process with relaxation time τ and diffusion

constant c . The importance of *Ornstein-Uhlenbeck* process lies in the successful mathematical descriptions of some typical physical systems with fluctuation-dissipation nature, which includes Brownian motion mentioned in the



former subsection. With the help of Eq. (1.1.10), we can transform Eqs. (1.1.5) and

(1.1.8) into

$$X(t+dt) = X(t) - \frac{1}{\tau}X(t)dt + \sqrt{c}N(t)\sqrt{dt} \quad , \quad (1.1.11)$$

$$\frac{dX(t)}{dt} = -\frac{1}{\tau}X(t) + \sqrt{c}\Gamma(t) \quad . \quad (1.1.12)$$

The above two equations are known as the equivalent forms of the *Langevin* equation

for the *Ornstein-Uhlenbeck* process. Being subject to the initial condition:

$X(t_0) = x_0$, $X(t+dt)$ in Eq. (1.1.11) can be expressed as a linear combination of

two normal random variables $X(t)$ and $N(t)$ since $X(t_0) = x_0 = N(x_0, 0)$ and

$N(t) = N(0,1)$. Hence, according to Eqs. (1.1.7a) and (1.1.7b), $X(t_0 + dt)$ must be normal. Next, $X(t_0 + 2dt)$ must also be normal since it is also a linear combination of two normal random variables $X(t_0 + dt)$ and $N(t_0 + dt)$. The same procedure is repeated. Ultimately, we can conclude that the random variable $X(t)$ in **Ornstein-Uhlenbeck** process is normal for all $t > t_0$.

To discover the solution of Eqs. (1.1.11) and (1.1.12) implies to find the mean and variance of the normal random variable $X(t)$ since the statistical behavior of a normal random variable can be completely determined by its mean and variance. To get the mean and variance of $X(t)$, let us take the average of Eq. (1.1.11) first, which yields $\langle X(t + dt) \rangle = \langle X(t) \rangle - \frac{1}{\tau} \langle X(t) \rangle dt$. The term of $\langle \sqrt{c} N(t) \sqrt{dt} \rangle$ vanishes in deriving the above equation because of $N(t) = N(0,1)$. By letting $dt \rightarrow 0$, we obtain a simple first order ordinary differential equation of $\langle X(t) \rangle$, whose solution for the initial condition $\langle X(t_0) \rangle = x_0$ is

$$\langle X(t) \rangle = x_0 \exp\left(-\frac{t-t_0}{\tau}\right), \quad t \geq t_0. \quad (1.1.13)$$

Next, in order to get the information about variance, we square Eq. (1.1.11) to obtain

$X^2(t + dt) = X^2(t) - \frac{2}{\tau} X^2(t) dt + 2\sqrt{c} X(t) N(t) \sqrt{dt} + cN^2(t) dt$. By averaging the equation, we then obtain $\langle X^2(t + dt) \rangle = \langle X^2(t) \rangle - \frac{2}{\tau} \langle X^2(t) \rangle dt + c dt$. Note that $\langle 2\sqrt{c} X(t) N(t) \sqrt{dt} \rangle = 2\sqrt{c} \langle X(t) \rangle \langle N(t) \rangle \sqrt{dt} = 0$ because of the statistical independency of $X(t)$ and $N(t)$, and $\langle N^2(t) \rangle = 1$ from $N(t) = N(0,1)$. Let

$dt \rightarrow 0$, the equation transforms into a first order O.D.E of $\langle X^2(t) \rangle$, whose solution for the initial condition $\langle X^2(t_0) \rangle = x_0^2$ can be easily derived to give $\langle X^2(t) \rangle = \left(x_0^2 - \frac{c\tau}{2} \right) e^{-2(t-t_0)/\tau} + \frac{c\tau}{2}$. Using this solution together with the help of Eq. (1.1.13), the variance of $X(t)$ can be obtained as follows

$$\text{var}\{X(t)\} = \langle X^2(t) \rangle - \langle X(t) \rangle^2 = \frac{c\tau}{2} \left(1 - e^{-2(t-t_0)/\tau} \right), \quad t \geq t_0. \quad (1.1.14)$$

Therefore from Eqs. (1.1.13) and (1.1.14) with the initial condition $X(t_0) = x_0$, we can conclude that the *Ornstein-Uhlenbeck* process with relaxation time τ and diffusion constant c is

$$X(t) = N \left(x_0 e^{-(t-t_0)/\tau}, \frac{c\tau}{2} \left(1 - e^{-2(t-t_0)/\tau} \right) \right), \quad t \geq t_0. \quad (1.1.15)$$

Furthermore, by some routine calculations, we can derive a limit equation as follows

$$\lim_{t-t_0 \rightarrow \infty} \text{var} \left\{ \int_{t_0}^t X(t') dt' \right\} = c\tau^2 (t - t_0), \quad (1.1.16)$$

which is also useful in the following formulae derivation.

1.1.3 Derivation of the Fluctuation-Dissipation Theorem (FDT) of a Physical System

Having attained the basic cognitions of stochastic process in subsection 1.1.2, we can proceed with the analysis of Brownian motion in a more systematic way. Let us return to the discussion in subsection 1.1.1. For simplicity, let us assume there does not exist any external force. Eq. (1.1.4) becomes $m \frac{dv}{dt} = -\gamma v + \tilde{F}(t)$. To take advantage of the well-developed *Ornstein-Uhlenbeck* process, we first transform the

above equation into the form

$$\frac{dv(t)}{dt} = -\frac{1}{m/\gamma}v(t) + m^{-1}\tilde{F}(t) . \quad (1.1.17)$$

We then define m/γ as a positive constant τ and $\tilde{F}(t)$ as $m\sqrt{c}\Gamma(t)$, Eq. (1.1.17)

would become

$$\frac{dv(t)}{dt} = -\frac{1}{\tau}v(t) + \sqrt{c}\Gamma(t) . \quad (1.1.18)$$

This is essentially the white-noise form of *Langevin* equation mentioned in subsection 1.1.2, and $v(t)$ is no other than an *Ornstein-Uhlenbeck* process with relaxation time τ and diffusion constant c . Here, we set the velocity of Brownian

particle as a normal random variable. Based on classical statistical thermodynamics, the velocity of Brownian particle must eventually be distributed in Maxwellian fashion. Now that $v(t)$ is purely a normal random variable in an

Ornstein-Uhlenbeck process, solving Eq. (1.1.17) becomes a simple task with the knowledge developed in subsection 1.1.2. The solution would then be of the form of

Eq. (1.1.15), which gives

$$v(t) = N\left(v_0 e^{-(t-t_0)/\tau}, \frac{c\tau}{2}\left(1 - e^{-2(t-t_0)/\tau}\right)\right), \quad t \geq t_0 . \quad (1.1.19)$$

It yields $v(t \rightarrow \infty) = N\left(0, \frac{c\tau}{2}\right)$. On the other hand, according to equipartition theorem,

the energy associated with fluctuation in each degree of freedom is $k_B T/2$, that is,

$\frac{1}{2}m \cdot \text{var}\{v(t \rightarrow \infty)\} = \frac{1}{2}k_B T$, we then have

$$\frac{c\tau}{2} = \frac{k_B T}{m} . \quad (1.1.20a)$$

By solving *Fick's* second law of diffusion, *Einstein* deduced that the mean-square displacement of Brownian particle from diffusion equation is $\langle x^2(t) \rangle = 2D(t - t_0)$.

Here, D is the diffusion coefficient of the diffusion equation. By comparing this

Einstein-derived equation with Eq. (1.1.16) we can find

$$2D = c\tau^2 \quad . \quad (1.1.20b)$$

By solving Eqs. (1.1.20a) and (1.1.20b) simultaneously, we have

$$\tau = \frac{Dm}{k_B T} \quad , \quad (1.1.21a)$$

$$c = \frac{2}{D} \left(\frac{k_B T}{m} \right)^2 \quad . \quad (1.1.21b)$$

Now, we are capable of examining the fluctuation-dissipation relation of Brownian motion in a quantitative way. Firstly, by substituting Eq. (1.1.21a) into τ which is

defined as $\frac{m}{\gamma}$, we get

$$\frac{m}{\gamma} = \frac{Dm}{k_B T} \quad \Rightarrow \quad \gamma = \frac{k_B T}{D} \quad . \quad (1.1.22)$$

From this formula, we can find that the diffusion coefficient D is related to the

friction constant. The above theoretical derivation also matches the experimental

observation discovered by *Einstein* very well. Second, by substituting Eq. (1.1.21b)

into $\tilde{F}(t) = m\sqrt{c}\Gamma(t)$ mentioned in the previous context together with Eq. (1.1.22),

we obtain $\tilde{F}(t) = \sqrt{2k_B T \gamma} \Gamma(t)$, which can be expressed in an alternative form

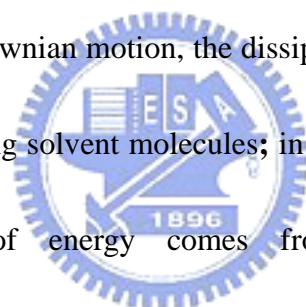
$$\langle \tilde{F}(t) \tilde{F}(t+t') \rangle = 2k_B T \gamma \delta(t') \quad , \quad (1.1.23)$$

by using Eq. (1.1.9b) in the derivation process. To gain a more deep insight into Eq.

(1.1.23), we integrate this equation to obtain

$$\gamma = \frac{1}{2k_B T} \int_{-\infty}^{\infty} \langle \tilde{F}(t) \tilde{F}(t+t') \rangle dt' . \quad (1.1.24)$$

This equation relates the fluctuating force $\tilde{F}(t)$ to the friction coefficient γ and is thus called the “*fluctuation-dissipation theorem*” . In a much more comprehensible picture, when a physical system shows fluctuating dynamics in some property, there must have some type of energy dissipation channel accompanying that physical property. We even can say that if there is no dissipation of energy there shall be no fluctuation. This inherent relationship between fluctuation and dissipation of energy is universally ubiquitous. In Brownian motion, the dissipation of energy comes from the head-on impact by surrounding solvent molecules; in molecular fluctuations in liquid crystals, the dissipation of energy comes from jostling by surrounding random-oriented molecules, and this case will be the main theme in later chapters.



1.2 Light Scattering from a Physical System

1.2.1 Basic Concepts of Light Scattering

In semi-classical physics, light is no other than an electromagnetic wave. When light impinges on matter, due to its electromagnetic nature, the oscillating electric field of the light induces an oscillating polarization of the electrons in the molecules. This oscillation of electrons infers the existence of acceleration of charged particles,

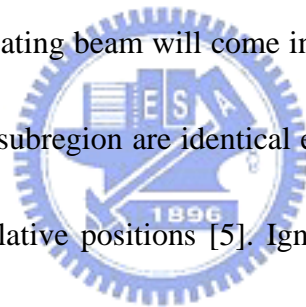
according to electromagnetic theory, which will re-radiate electromagnetic wave in all directions. The incident optical field is said to polarize the medium [5]. The molecules then serve as secondary sources of light and this reradiation is known as light scattering [6].

Generally speaking, there are two basic types of light scattering, named in honor of two Nobel Prize Laureates in physics, **Chandrasekhara V. Raman** (1888–1970) and **Lord Rayleigh** (1842–1919). When photons impinge on a molecule, they can either impart energy to or gain energy from the molecule. This energy transfer could be associated with the translational, rotational, vibrational, or electronic degrees of freedom of the molecules [6]. These photons thereby experience frequency shifts and the scattering is thus *inelastic*. Light scattering in such a way is called **Raman scattering**.

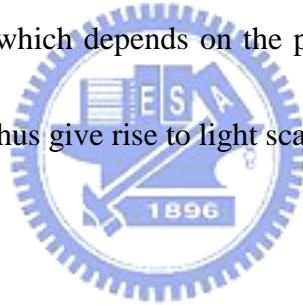
The other type of light scattering is **Rayleigh scattering**. In the following, we shall proceed to investigate the angular dependence, the polarization and the intensity of the quasi-elastically scattered light. In this case the frequency spectrum of the scattered light is broadened by a small frequency shift due to a distribution of finite lifetime of thermal fluctuations in the medium that scatter light [6]. Nevertheless, the central frequency of the spectrum is not shifted as it should be in quasi-elastic regime. In this thesis, we shall make a good use of this quasi-elastic light scattering technique

to probe certain intriguingly dynamical physical systems in the later content.

Let's probe further deep into the physical picture of light scattering. When light is incident upon the medium to yield an illuminated volume, the atoms in a subregion, which is small compared with the scale of the incident light wavelength, shall see the same incident optical field strength. When these subregions with equal size are considered to produce the optical scattering effect, the total scattered field shall be the superposition of the scattered optical fields from each of them. If these subregions are all optically identical, that is, each has the same dielectric constant, no scattered light other than the forward-propagating beam will come into being. This is so because the wavelets scattered from each subregion are identical except for their individual phase factor that depends on the relative positions [5]. Ignoring the surface effects of the medium, each subregion can always be paired with another one whose scattered electric field is identical in amplitude but opposite in phase and thus will cancel out, leaving no net scattered light in other than the forward direction. However, if these subregions are not optically identical, that is, they have different dielectric constants, then the amplitudes of the light scattered from different subregions are no longer identical. For this reason, complete cancellation of electric field in other than the forward direction will not happen any longer. This is the reason why there exists scattered light in other than the forward direction after incident light impinges on an



optically inhomogeneous medium. According to this semi-macroscopic view, originally brought up by *Einstein*, scattered light arises from optical inhomogeneity and the optical inhomogeneity results from local fluctuations in the dielectric constant of the medium (*Einstein*, 1910). From Section 1.1, we know the fact that all thermodynamic quantities show unavoidable fluctuation behavior governed by their own fluctuation-dissipation theorem. On a microscopic view, kinetic theory tells us that molecules in any given medium are not at rest, they are constantly vibrating, rotating and even translating. Therefore any given subregion's physical quantities (such as dielectric constant), which depends on the positions and orientations of the molecules, will fluctuate and thus give rise to light scattering.



1.2.2 Electromagnetic Theory of Light Scattering

First, let us consider a nonmagnetic, nonconducting and nonabsorbing dielectric medium with average dielectric constant ϵ_0 . An incident plane wave with amplitude E_0 , wave vector \vec{k}_i , angular frequency ω_i and the unit vector \hat{n}_i pointing toward the direction of the incident electric field can be properly described as $\vec{E}_i = \hat{n}_i E_0 \exp i(\vec{k}_i \cdot \vec{r} - \omega_i t)$. The medium on which the optical wave is impinged has a local dielectric constant $\vec{\epsilon}(\vec{r}, t) = \epsilon_0 \vec{I} + \delta\vec{\epsilon}(\vec{r}, t)$, where \vec{I} denotes the second-rank unit tensor and $\delta\vec{\epsilon}(\vec{r}, t)$ is the thermally fluctuating part of dielectric tensor [6]. If the

EM fields of the incident plane wave are described by \vec{E}_i , \vec{D}_i , \vec{B}_i , \vec{H}_i and the scattered fields are represented as \vec{E}_s , \vec{D}_s , \vec{B}_s , \vec{H}_s , the total fields at a position in the scattering medium can then be expressed as

$$\begin{aligned}\vec{E} &= \vec{E}_i + \vec{E}_s \quad , \\ \vec{D} &= \vec{D}_i + \vec{D}_s \quad , \\ \vec{B} &= \vec{B}_i + \vec{B}_s \quad , \\ \vec{H} &= \vec{H}_i + \vec{H}_s \quad .\end{aligned}\tag{1.2.1}$$

Since the incident fields and the total fields all satisfy the Maxwell equations, the scattered fields shall also obey the Maxwell equations [5]. The Maxwell's equations for the scattered fields in the absence of sources are

$$\vec{\nabla} \times \vec{E}_s = -\frac{\partial \vec{B}_s}{\partial t} \quad ,\tag{1.2.2a}$$

$$\vec{\nabla} \times \vec{H}_s = \frac{\partial \vec{D}_s}{\partial t} \quad ,\tag{1.2.2b}$$

$$\vec{\nabla} \cdot \vec{B}_s = 0 \quad , \quad \vec{\nabla} \cdot \vec{D}_s = 0 \quad .\tag{1.2.2c}$$

By taking curl of Eq. (1.2.2a) and then combining with Eq. (1.2.2b), we obtain

$$\vec{\nabla} \times \vec{\nabla} \times \vec{E}_s = -\frac{\partial \vec{\nabla} \times \vec{B}_s}{\partial t} = -\mu \frac{\partial \vec{\nabla} \times \vec{H}_s}{\partial t} = -\mu \frac{\partial^2}{\partial t^2} \vec{D}_s \quad .\tag{1.2.3}$$

The total electric displacement vector \vec{D} and the total electric field vector \vec{E} are related through the dielectric constant $\vec{\epsilon}(\vec{r}, t) = \epsilon_0 \vec{I} + \delta\vec{\epsilon}(\vec{r}, t)$ by

$$\begin{aligned}\vec{D} &= (\epsilon_0 \vec{I} + \delta\vec{\epsilon}) \cdot (\vec{E}_i + \vec{E}_s) \\ &= \epsilon_0 \vec{E}_i + \delta\vec{\epsilon} \cdot \vec{E}_i + \epsilon_0 \vec{E}_s + \delta\vec{\epsilon} \cdot \vec{E}_s \quad .\end{aligned}\tag{1.2.4}$$

From Eq. (1.2.1) and the fact that $\vec{D}_i = \epsilon_0 \vec{E}_i$, Eq. (1.2.4) gives

$$\vec{D}_s = \epsilon_0 \vec{E}_s + \delta\vec{\epsilon} \cdot \vec{E}_i \quad .\tag{1.2.5}$$

In the above derivation we have neglected the second-order term $\delta\vec{\mathcal{E}} \cdot \vec{E}_s$. By solving

Eq. (1.2.5) for \vec{E}_s and then substituting the result into Eq. (1.2.3) together with the

assumption of a nonmagnetic medium, we obtain $\vec{\nabla} \times \vec{\nabla} \times (\vec{D}_s - \delta\vec{\mathcal{E}} \cdot \vec{E}_i) = -\mu_0 \epsilon_0 \frac{\partial^2}{\partial t^2} \vec{D}_s$.

By using the vector identity $\vec{\nabla} \times \vec{\nabla} \times \vec{a} = \vec{\nabla}(\vec{\nabla} \cdot \vec{a}) - \vec{\nabla}^2 \vec{a}$ and making some algebraic

rearrangement, we obtain an inhomogeneous wave equation

$$\vec{\nabla}^2 \vec{D}_s - \mu_0 \epsilon_0 \frac{\partial^2}{\partial t^2} \vec{D}_s = -\vec{\nabla} \times \vec{\nabla} \times \delta\vec{\mathcal{E}} \cdot \vec{E}_i . \quad (1.2.6)$$

To simplify the above wave equation, we define the **Hertz** vector $\vec{\Pi}$ by

$\vec{D}_s = \vec{\nabla} \times \vec{\nabla} \times \vec{\Pi}$ [5]. Taking this defined-form into Eq. (1.2.6) leads to

$$\begin{aligned} & \vec{\nabla}^2 (\vec{\nabla} \times \vec{\nabla} \times \vec{\Pi}) - \mu_0 \epsilon_0 \frac{\partial^2}{\partial t^2} \vec{\nabla} \times \vec{\nabla} \times \vec{\Pi} = -\vec{\nabla} \times \vec{\nabla} \times \delta\vec{\mathcal{E}} \cdot \vec{E}_i \\ \Rightarrow & \vec{\nabla}^2 \vec{\Pi} - \mu_0 \epsilon_0 \frac{\partial^2}{\partial t^2} \vec{\Pi} = -\delta\vec{\mathcal{E}} \cdot \vec{E}_i . \end{aligned} \quad (1.2.7)$$

The above Hertzian wave equation is exactly in the standard form of d'Alembert

differential equation, $\vec{\nabla}^2 F(\vec{r}, t) - \frac{1}{c^2} \frac{\partial^2 F(\vec{r}, t)}{\partial t^2} = \Phi(\vec{r}, t)$, which yields a general solution of

$F(\vec{r}, t) = -\frac{1}{4\pi} \int_{V'} \frac{\Phi(\vec{r}', t - \frac{1}{c} |\vec{r} - \vec{r}'|)}{|\vec{r} - \vec{r}'|} dV'$. Therefore we can solve Eq. (1.2.7) to yield the

scattered electric field $\vec{E}_s(\vec{r}, t)$ outside the medium ($\epsilon = \epsilon_0$)

$$\begin{aligned} \vec{E}_s(\vec{r}, t) &= \frac{\vec{D}_s(\vec{r}, t)}{\epsilon_0} = \frac{\vec{\nabla} \times \vec{\nabla} \times \vec{\Pi}}{\epsilon_0} \\ &= \frac{\vec{\nabla} \times \vec{\nabla} \times}{\epsilon_0} \left\{ -\frac{1}{4\pi} \int_{V'} d^3 r' \frac{-\delta\vec{\mathcal{E}}(\vec{r}', t') \cdot \hat{n}_i E_0 e^{i(\vec{k}_i \cdot \vec{r}' - \omega_i t')}}{|\vec{r} - \vec{r}'|} \Bigg|_{t'=t-\frac{|\vec{r}-\vec{r}'|}{c}} \right\} \\ &= \frac{\vec{\nabla} \times \vec{\nabla} \times}{4\pi\epsilon_0} \left\{ \int_{V'} d^3 r' \frac{\delta\vec{\mathcal{E}}(\vec{r}', t') \cdot \hat{n}_i E_0 e^{i(\vec{k}_i \cdot \vec{r}' - \omega_i t')}}{|\vec{r} - \vec{r}'|} \Bigg|_{t'=t-\frac{|\vec{r}-\vec{r}'|}{c}} \right\} . \end{aligned} \quad (1.2.8)$$

V' denotes the scattering volume (see Fig. 1-2-1), t' means the scattering time occurring at \vec{r}' , and is observed at \vec{r} and time t . The time difference $t-t'$ is just the time duration required for the electromagnetic disturbance to propagate a distance from \vec{r}' to \vec{r} .

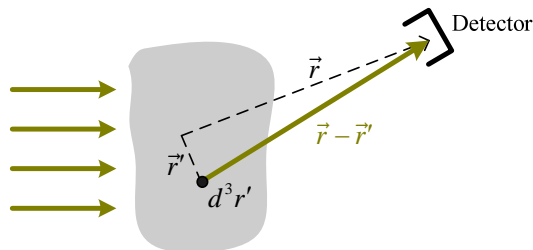


Fig. 1-2-1 The total radiated field observed at Detector is the superposition of those radiated from all infinitesimal elements d^3r' at positions \vec{r}' with respect to the center of the illuminated volume [5].

Since the detector is distant from the scattering medium, $|\vec{r} - \vec{r}'|$ can be expanded in a power series

$$\begin{aligned}
 |\vec{r} - \vec{r}'| &= \sqrt{(\vec{r} - \vec{r}') \cdot (\vec{r} - \vec{r}')} = \sqrt{r^2 - 2\vec{r} \cdot \vec{r}' + r'^2} \\
 &\xrightarrow{|\vec{r}'| \ll |\vec{r}|} \\
 &\approx r \sqrt{1 - 2\frac{\vec{r} \cdot \vec{r}'}{r^2}} \approx r \left(1 - \frac{\vec{r} \cdot \vec{r}'}{r^2} \right) = r - \hat{k}_f \cdot \vec{r}' = \hat{k}_f \cdot (\vec{r} - \vec{r}') ,
 \end{aligned} \tag{1.2.9}$$

where \hat{k}_f is a unit vector in the direction of \vec{r} . Then the following results are obtained

$$t' \approx t - \frac{1}{c} \hat{k}_f \cdot (\vec{r} - \vec{r}') , \tag{1.2.10}$$

$$\frac{1}{|\vec{r} - \vec{r}'|} \approx \frac{1}{r - \hat{k}_f \cdot \vec{r}'} = \frac{1}{r} \left[1 + \frac{\hat{k}_f \cdot \vec{r}'}{r} + \frac{(\hat{k}_f \cdot \vec{r}')^2}{r^2} + \dots \right] \approx \frac{1}{r} . \tag{1.2.11}$$

Substituting Eqs. (1.2.9), (1.2.10) and (1.2.11) into Eq. (1.2.8) and using $k_i = \frac{\omega_i}{c} \approx k_f$,

we finally have

$$\begin{aligned}
\vec{E}_s(\vec{r}, t) &= \frac{\vec{\nabla} \times \vec{\nabla} \times}{4\pi\epsilon_0} \left\{ \int_{V'} d^3r' \frac{\delta\vec{\mathcal{E}}(\vec{r}', t') \cdot \hat{n}_i E_0 e^{i[\vec{k}_i \cdot \vec{r}' - \omega_i \cdot (t - \frac{1}{c}\hat{k}_f \cdot (\vec{r} - \vec{r}'))]}}{|\vec{r} - \vec{r}'|} \right\} \\
&= \frac{\vec{\nabla} \times \vec{\nabla} \times}{4\pi\epsilon_0} \left\{ \int_{V'} d^3r' \frac{\delta\vec{\mathcal{E}}(\vec{r}', t') \cdot \hat{n}_i E_0 e^{i[\vec{k}_i \cdot \vec{r}' - \omega_i \cdot t + \frac{\omega_i}{c}\hat{k}_f \cdot (\vec{r} - \vec{r}')]}}{r} \right\} \\
&= \frac{\vec{\nabla} \times \vec{\nabla} \times}{4\pi\epsilon_0 r} \left\{ \int_{V'} d^3r' \delta\vec{\mathcal{E}}(\vec{r}', t') \cdot \hat{n}_i E_0 e^{i[\vec{k}_i \cdot \vec{r}' - \omega_i \cdot t + \vec{k}_f \cdot (\vec{r} - \vec{r}')]}} \right\} \\
&= \frac{E_0}{4\pi\epsilon_0 r} \left\{ \vec{\nabla}_{\vec{r}} \times \vec{\nabla}_{\vec{r}} \times \int_{V'} d^3r' \delta\vec{\mathcal{E}}(\vec{r}', t') \cdot \hat{n}_i e^{i(\vec{k}_f \cdot \vec{r} - \omega_i \cdot t)} e^{i(\vec{k}_i - \vec{k}_f) \cdot \vec{r}'} \right\} \\
&= \frac{E_0}{4\pi\epsilon_0 r} e^{i(\vec{k}_f \cdot \vec{r} - \omega_i \cdot t)} \left\{ \vec{k}_f \times \vec{k}_f \times \int_{V'} d^3r' \delta\vec{\mathcal{E}}(\vec{r}', t') \cdot \hat{n}_i e^{i(\vec{k}_i - \vec{k}_f) \cdot \vec{r}'} \right\} \\
&= \frac{E_0}{4\pi\epsilon_0 r} e^{i(\vec{k}_f \cdot \vec{r} - \omega_i \cdot t)} \left\{ \int_{V'} d^3r' e^{i(\vec{k}_i - \vec{k}_f) \cdot \vec{r}'} \vec{k}_f \times \vec{k}_f \times \delta\vec{\mathcal{E}}(\vec{r}', t') \cdot \hat{n}_i \right\} \\
&= \frac{E_0}{4\pi\epsilon_0 r} e^{i(\vec{k}_f \cdot \vec{r} - \omega_i \cdot t)} \int_{V'} d^3r' e^{i\vec{q} \cdot \vec{r}'} \vec{k}_f \times \vec{k}_f \times \delta\vec{\mathcal{E}}(\vec{r}', t') \cdot \hat{n}_i .
\end{aligned}$$

The scattering vector \vec{q} is defined as $\vec{q} \equiv \vec{k}_i - \vec{k}_f$, where \vec{k}_i and \vec{k}_f point in the direction of the incident wave and the wave toward the detector, respectively.

Intuitively, we can view \vec{q} as the electromagnetic momentum transfer in the process of light scattering [7].

In general, scattered light is detected with polarization \hat{n}_f to reveal dynamics of specific degree of freedom. Hence, the scattered field observed at the detector is given by

$$E_s(\vec{r}, t) = \hat{n}_f \cdot \vec{E}_s(\vec{r}, t)$$

$$\begin{aligned}
&= \hat{n}_f \cdot \frac{E_0}{4\pi\epsilon_0 r} e^{i(\vec{k}_f \cdot \vec{r} - \omega_i t)} \int_{V'} d^3 r' e^{i\vec{q} \cdot \vec{r}'} \vec{k}_f \times \vec{k}_f \times \delta\vec{\epsilon}(\vec{r}', t') \cdot \hat{n}_i \\
&= \frac{k_f^2 E_0}{4\pi\epsilon_0 r} e^{i(\vec{k}_f \cdot \vec{r} - \omega_i t)} \int_{V'} d^3 r' e^{i\vec{q} \cdot \vec{r}'} \hat{n}_f \cdot \hat{k}_f \times \hat{k}_f \times \delta\vec{\epsilon}(\vec{r}', t) \cdot \hat{n}_i \quad . \quad (1.2.12)
\end{aligned}$$

The element $\delta\epsilon_{if}(\vec{r}, t)$ of the dielectric fluctuation tensor is defined as

$$\begin{aligned}
\delta\epsilon_{if} &= \hat{n}_f \cdot \hat{k}_f \times \hat{k}_f \times \delta\vec{\epsilon} \cdot \hat{n}_i \\
&= \hat{n}_f \cdot \left[\hat{k}_f \left(\hat{k}_f \cdot \delta\vec{\epsilon} \cdot \hat{n}_i \right) - \delta\vec{\epsilon} \cdot \hat{n}_i \right] \\
&= \underbrace{\hat{n}_f \cdot \hat{k}_f}_{=0} \left(\hat{k}_f \cdot \delta\vec{\epsilon} \cdot \hat{n}_i \right) - \hat{n}_f \cdot \delta\vec{\epsilon} \cdot \hat{n}_i \\
&= -\hat{n}_f \cdot \delta\vec{\epsilon} \cdot \hat{n}_i \quad .
\end{aligned}$$

Here we took advantage of the bac-cab rule and the fact that final polarization must be orthogonal to the scattered wave vector, *i.e.*, $\hat{n}_f \cdot \hat{k}_f = 0$. Accordingly, Eq. (1.2.12) is

further simplified to

$$E_s(\vec{r}, t) = \frac{k_f^2 E_0}{4\pi\epsilon_0 r} e^{i(\vec{k}_f \cdot \vec{r} - \omega_i t)} \int_{V'} d^3 r' e^{i\vec{q} \cdot \vec{r}'} \delta\epsilon_{if}(\vec{r}', t) \quad . \quad (1.2.13)$$

From the above, it is clear that the existence of the dielectric fluctuation will induce light scattering away from the direction of the incident wave.

1.3 Autocorrelation Function of Scattered Photons from a Physical System

1.3.1 Basic Concepts of Autocorrelation Function

Correlation function is measure of the similarity between two arbitrary signal waveforms [5, 7]. It provides a concise way of expressing the degree to which two

dynamical properties are correlated over a period of time. We shall discuss some features of correlation functions that are helpful to understand the essence of the signals from photocounts read by photodetector and to extract certain relevant dynamical information of the corresponding physical systems.

To begin with, let us consider a physical property $Y(\{r_i\},\{p_i\})$ that depends on the positions $\{r_i\}$ and momenta $\{p_i\}$ of all the components (they can be particles, molecules, *etc.*) in the system. By virtue of their thermal motions, these small components are constantly shoving with each other so that their positions and momenta are constantly changing in time, and so is the corresponding property Y . It is important to declare that although every single component must obey Newton's laws of motion, their massive quantity makes their thermal motions appear to be somewhat random. We can view them as stochastic process legitimately, and this stochastic nature leads to erratic behavior of the property Y , that is fluctuation. In statistics, the most efficient way to extract information from a stochastic property is through its autocorrelation function.

Generally, the stochastic and fluctuated property Y will show a noise-like profile due to its random behavior (Fig. 1-3-1).

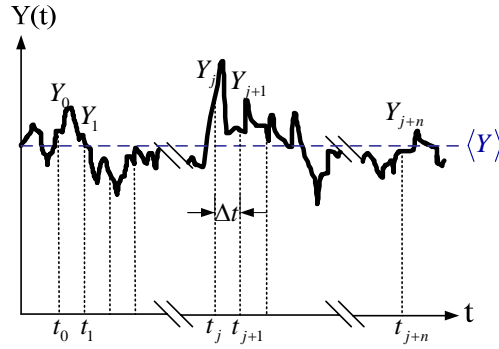


Fig. 1-3-1 Typical noise-like pattern of a physical property Y . The time axis is divided into discrete intervals, Δt in width, and $\langle Y \rangle$ means the time average of Y .

The noise-like signal $Y(t)$ possesses the following features : the property Y usually takes on different values at different positions in time axis, that is, $Y(t+\tau) \neq Y(t)$, provided that $\tau \neq 0$. However, when τ is small compared with the time scale characterizing the fluctuations in Y , $Y(t+\tau)$ will be very close to $Y(t)$. As τ increases, $Y(t+\tau)$ and $Y(t)$ are likely getting less and less similar. With this notion in mind, we can say that $Y(t+\tau)$ and $Y(t)$ are correlated when τ is small, whereas $Y(t+\tau)$ and $Y(t)$ are getting less and less correlated as τ is getting larger. To specify this phenomenon more quantitatively, we need a measure of this correlation. An efficient and viable method is the autocorrelation function of the property Y which is defined as

$$\langle Y(0)Y(\tau) \rangle \equiv \lim_{T \rightarrow \infty} \frac{1}{T} \int_0^T dt Y(t)Y(t+\tau) . \quad (1.3.1)$$

Here, a fact must be reminded that for time-invariant property, the corresponding

autocorrelation function possesses a feature as follows, $\langle Y(t)Y(t+\tau) \rangle = \langle Y(0)Y(\tau) \rangle$.

In order to make the calculation of Eq. (1.3.1) workable, we discretize the time axis into discrete intervals with Δt in width, such that $t_j = j\Delta t$, $\tau = n\Delta t$, and $T = N\Delta t$.

Next, we replace integration with summation, and then Eq. (1.3.1) becomes

$\langle Y(0)Y(\tau) \rangle \cong \lim_{N \rightarrow \infty} \frac{1}{N} \sum_{j=1}^N Y_j Y_{j+n}$. Here Y_j denotes the j^{th} value of the property Y ,

which is counted from the beginning to the j^{th} interval. We are interested in how the autocorrelation function behaves or how it varies with time. To answer these questions,

we must acquaint ourselves with the principle of **Schwartz's** inequality [5] in advance,

which states that $\left| \sum_j X_j Y_j \right|^2 \leq \left(\sum_j X_j^2 \right) \left(\sum_j Y_j^2 \right)$. Let us now take $X_j = Y_{j+n}$, divide both

sides by N^2 and take the limit $N \rightarrow \infty$, the above **Schwartz's** inequality will lead to

$\left| \lim_{N \rightarrow \infty} \frac{1}{N} \sum_{j=1}^N Y_j Y_{j+n} \right|^2 \leq \left(\lim_{N \rightarrow \infty} \frac{1}{N} \sum_{j=1}^N Y_j^2 \right) \left(\lim_{N \rightarrow \infty} \frac{1}{N} \sum_{j=1}^N Y_{j+n}^2 \right) = \left(\lim_{N \rightarrow \infty} \frac{1}{N} \sum_{j=1}^N Y_j^2 \right)^2$. What the above

inequality implies is that $\lim_{N \rightarrow \infty} \frac{1}{N} \sum_{j=1}^N Y_j Y_{j+n} \leq \lim_{N \rightarrow \infty} \frac{1}{N} \sum_{j=1}^N Y_j^2$ or $\langle Y(0)Y(\tau) \rangle \leq \langle Y(0)^2 \rangle$.

This result tell us an important feature of the autocorrelation function, namely,

delayed autocorrelation value (*i.e.*, $\tau \neq 0$) will never exceed initial autocorrelation

value (*i.e.*, $\tau = 0$). To be more explicit, we would say that the autocorrelation

function of a nonconserved, nonperiodic property decays from its initial value $\langle Y^2 \rangle$.

For delays τ large compared with the characteristic time for the fluctuation of Y ,

$Y(t)$ and $Y(t+\tau)$ are expected to become completely uncorrelated [5]. That is to

say, $\lim_{\tau \rightarrow \infty} \langle Y(0)Y(\tau) \rangle = \langle Y(0) \rangle \langle Y(\tau) \rangle = \langle Y \rangle^2$. This means that the autocorrelation

function of a nonperiodic property decays from $\langle Y^2 \rangle$ to $\langle Y \rangle^2$ in the course of time.

Now that we have caught on some basic features of the autocorrelation function of certain physical property Y , we are capable of proceeding with further deeper discussion about practical properties, such as signals generated by photodetector after which receives photons impinging on it. In light scattering experiments, photodetectors, inclusive of photomultipliers (PMTs) and photodiodes (PDs), act as nonlinear square-law detectors [7]. Photons impinging on the photodetector produce amplified photonelectron current pulses at its output. However, we must stress that only a fraction of the input photons are responsible for the output photoelectron pulses.

Besides, the quantum efficiency of the photodetector must also be taken into account before the experiment is conducted. Because of the above two uncertain factors, the whole process of the detection of photons is a statistical process. Hence, we must

introduce probability to proceed with the analysis by the same token. The probability

distribution of sensing n photoelectron pulses by an ideal photodetector in a

sampling time interval T from t to $t+T$ is $p(n,t,T) = \left(\frac{1}{n!}\right) (\alpha \langle I \rangle T)^n e^{-\alpha \langle I \rangle T}$,

where α is a coefficient that is proportional to the quantum efficiency with which

the photons are capable of ejecting electrons as well as the effective gain of the

photodetector, *i.e.*, $\alpha = (\text{quantum efficiency}) \times (\text{photodetector gain})$, $\langle I \rangle$ is a

short-time average intensity, and T is the sampling time period. The average number

of photoelectron pulses emitted during the sampling period T is

$$\begin{aligned}
\langle n(T) \rangle &= \sum_{n=0}^{\infty} n \cdot p(n, t, T) = \sum_{n=0}^{\infty} \frac{n(\alpha \langle I \rangle T)^n}{n!} e^{-\alpha \langle I \rangle T} = \sum_{n=1}^{\infty} \frac{(\alpha \langle I \rangle T)^n}{(n-1)!} e^{-\alpha \langle I \rangle T} \\
&= e^{-\alpha \langle I \rangle T} (\alpha \langle I \rangle T) \sum_{n=1}^{\infty} \frac{(\alpha \langle I \rangle T)^{n-1}}{(n-1)!} \\
&= e^{-\alpha \langle I \rangle T} (\alpha \langle I \rangle T) e^{\alpha \langle I \rangle T} = \alpha \langle I \rangle T
\end{aligned}$$

With the help of the above relationship, we then get

$$\langle n(t)n(t+\tau) \rangle = \alpha^2 T^2 \langle I(t)I(t+\tau) \rangle = \alpha^2 T^2 \langle I(t) \rangle^2 g^{(2)}(\tau) , \quad (1.3.2)$$

where

$$g^{(2)}(\tau) = \frac{\langle E^*(t)E(t)E^*(t+\tau)E(t+\tau) \rangle}{\langle E^*(t)E(t) \rangle^2} = \frac{\langle I(t)I(t+\tau) \rangle}{\langle I(t) \rangle^2} \quad (1.3.3)$$

is the normalized intensity correlation function. At this moment, we reach an important conclusion: the intensity autocorrelation function can be completely determined by means of the photon-count autocorrelation function. That is to say, the information of the second-order correlation function $g^{(2)}(\tau)$ can be completely extracted from the information of the output of the photodetector.

1.3.2 Implementation of Autocorrelation Function

The most promising technique, which makes best use of the digital nature of photon statistics of scattered light, is photon-count autocorrelation function. The autocorrelation function of photoncounting fluctuations is related to the

autocorrelation function of the short-time-averaged intensity fluctuations by the relationship

$$\langle n(t)n(t+\tau) \rangle = \alpha^2 T^2 \langle I(t)I(t+\tau) \rangle = \alpha^2 T^2 \langle I(t) \rangle^2 g^{(2)}(\tau) , \quad (1.3.2)$$

where $n(t)$ is the number of photocounts (*i.e.*, photoelectron counts) during the time interval t to $t+T$ with T being the sampling time which satisfies the condition $T \ll \tau_c$, where τ_c is the characteristic decay time of photon-count or intensity fluctuations (not of the source). $I(t)$ is the short-time-averaged (over T) intensity of light incident on the photodetector at t . α is the effective quantum efficiency of the whole light-collecting system. This relationship allows us to get $\langle I(t)I(t+\tau) \rangle$ by simply measuring $\langle n(t)n(t+\tau) \rangle$.

There are several ways to measure $\langle n(t)n(t+\tau) \rangle$. In this thesis, all the measures are based on the digital correlator technique. Here, we shall discuss its basic operation principles. For a sequence of photoelectron pulses with $n(t_i)$ as random variables (due to its Poissonian nature), as shown in Fig. 1-3-2, the average product $M(\tau_\ell)$ corresponding to the specific delay time τ_ℓ for the photon-count autocorrelation function is defined by

$$M(\tau_\ell) = \frac{1}{N-\ell} \sum_{i=1}^{N-\ell} n(t_i)n(t_{i+\ell}), \quad \ell = 1, 2, 3, \dots, L \quad (1.3.4)$$

where $\tau_\ell = \ell T$ and $L \ll N$. N is the number of samples of counts measured over the total time duration NT with T being the sampling time interval for each n ;

L is the longest delay-time index with delay-time increment T so that the longest delay time $\tau_L = LT$. A clear example with a specific delay time $\tau_2 = 2T$ is shown in

Fig. 1-3-2.

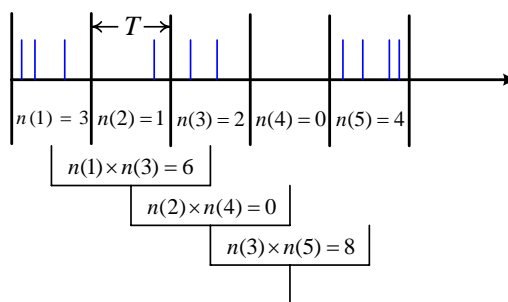


Fig. 1-3-2 Computation of the photoelectron-count autocorrelation function at stage $\tau_2 = 2T$. $n(t_i)$, denoted by $n(i)$, is the number of photocounts detected at time t_i over a sampling time T . In this case,

$$M(2T) = \left(\frac{1}{N-2}\right) \sum_{i=1}^{N-2} n(t_i)n(t_{i+2}) = \left(\frac{1}{N-2}\right)(6+0+8+\dots).$$

In our experiment, we use a digital correlator to carry out Eq. (1.3.4) and the whole implementation process is real-time since the data processing rate is generally high in state-of-the-art hardware correlators. Fig. 1-3-3 shows

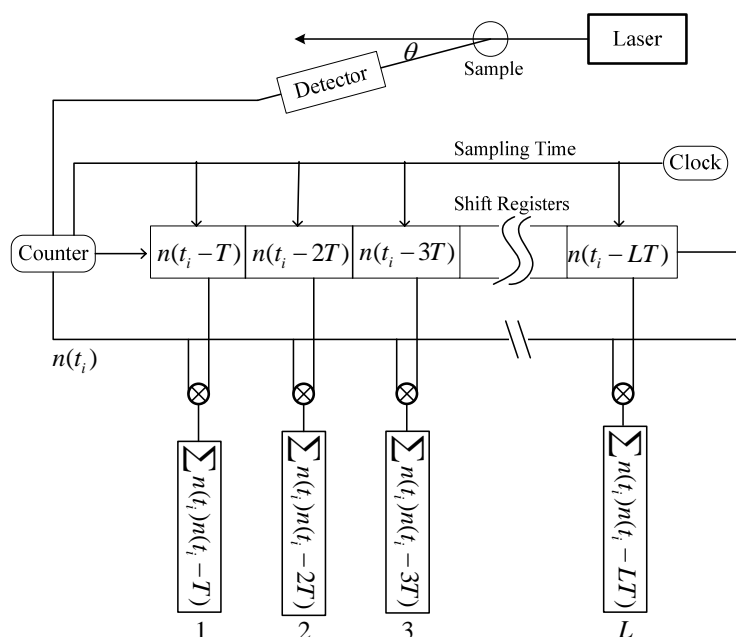


Fig. 1-3-3 Schematic illustration of Dynamic Light Scattering experiment and operation of the digital correlator. 1, 2, 3, ..., L are delay-time indices with delay-time increment T [7].

A digital correlator samples the incident signals from a photodetector. These sampled signals are converted into photonelectron pulses. By counting the number of these photonelectron pulses (referred to as photon events) occurring in a sample time T , we can get a train of counting numbers $n(t_i)$, $n(t_i + T)$, $n(t_i + 2T)$, ..., and then compute the average products corresponding to different delays as follows,

$$\begin{aligned}
 M(\tau_1 = T) &= \frac{1}{N-1} \sum_{i=1}^{N-1} n(t_i) n(t_{i+1}) , \\
 M(\tau_2 = 2T) &= \frac{1}{N-2} \sum_{i=1}^{N-2} n(t_i) n(t_{i+2}) , \\
 &\vdots \\
 M(\tau_L = LT) &= \frac{1}{N-L} \sum_{i=1}^{N-L} n(t_i) n(t_{i+L}) .
 \end{aligned} \tag{1.3.5}$$

In hardware correlator's internal logic, the input signal (equivalent to using $n(t_i)$) is routed into two paths with one path keeping $n(t_i)$ unchanged as a reference multiplier and the other path introducing multiple delays of the original $n(t_i)$, allowing all channels' multiplications in Eq. (1.3.5) to be performed in parallel, just like that shown in Fig. 1-3-3. Having completed all the implementation processes for realizing the calculation of Eq. (1.3.3), we can say that the goal of getting the autocorrelation function of the fluctuations from certain physical property has been presented successfully.

1.3.3 Test Run of Flex02-01D Digital Correlator

Flex02-01D is a state-of-the-art commercial correlator, which is made by Correlator.com. We use it in multiple tau mode to calculate autocorrelation function. The term “Multiple tau” means that it uses various delay-time differences between any two consecutive delay times, instead of a constant one in linear mode, to calculate Eq. (1.3.3). Multiple tau technique has the advantage of higher speed than that of single tau scheme since delay time advances in a hopping fashion. Moreover, the characteristics of 1.5625 ns minimum sampling time and 1152 real-time channels make Flex02-01D work precisely and efficiently. In this subsection, we shall demonstrate the measurement of identifying the hydrodynamic diameter of Au nanoparticles to verify the performance of Flex02-01D and our dynamic light scattering apparatus.

Before go into the technical details, let us first concisely discuss about how to determine the hydrodynamic diameter of the solute via the autocorrelation function measurement with dynamic light scattering [8,9,10]. Consider that a monochromatic plane wave is incident on the solution in which identical micrometer-scale particles undergo Brownian motion. The incident photons are scattered due to the optical inhomogeneity produced by the mixing of small particles and solvent. Far from the

scattering region, the radiation scattered from each particles is approximated by an outgoing spherical wave, which is shown in Fig. 1-3-4, and the electric field perceived by the detector will be the sum of the scattered spherical waves from all particles in the scattering region.

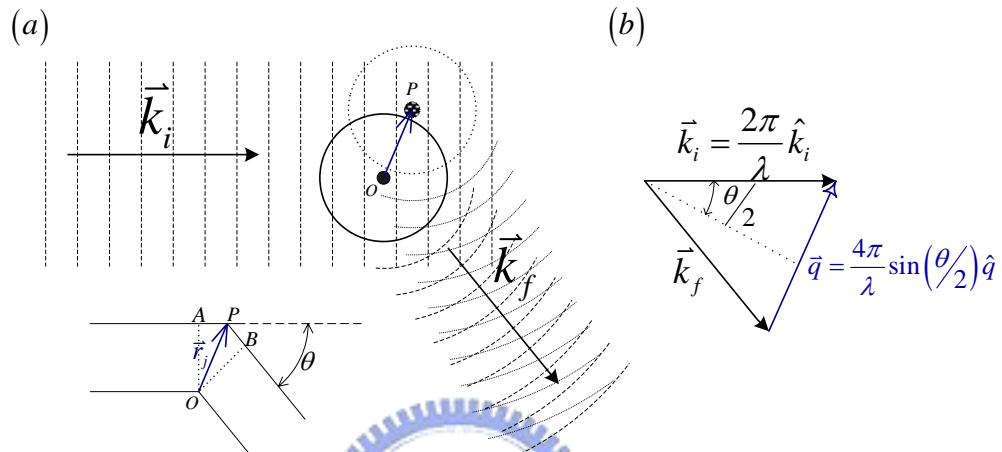


Fig. 1-3-4 (a) Incident plane waves (dotted lines) travel in the direction of \vec{k}_i . Spherical scattered wavefronts (dotted circles) from spheres are brought about. The detector will be placed in the direction of \vec{k}_f that is shown by interference of two particles' scattered spherical wave; O represents the reference sphere, and P represents another sphere located in \vec{r}_j relative to O [9]; (b) The scattering is quasi-elastic so that $|\vec{k}_i| = |\vec{k}_f|$ and $\vec{q} = 2|\vec{k}_i| \sin(\theta/2) \hat{q}$.

The scattered spherical wave from a stationary particle is of the form having typical sinusoidal electric field strength variation, $E_0 e^{i(\phi - \omega_0 t)}$, where E_0 is the amplitude of the oscillation that depends on various properties of the scattering system, such as incident wave's polarization, polarizabilities of the particles and solvent, and scattering angle, *etc.*; ω_0 is the angular frequency of the oscillation that is the same as that of the incident plane wave. If the detector is far from the scattering volume, the

variations in E_0 from particles at different positions are negligible. That is, E_0 can be considered as a constant for all identical particles observed at a single scattering angle. However, ϕ is highly sensitive to the position of the scatterer and would suffer severe 2π change even when the particle moves in a distance as short as a wavelength. Variations in ϕ as the particles move about lead to variations in the electric field strength and are thus the source of the intensity fluctuation to be measured in this experiment.

In Fig. 1-3-4 (a), O is taken as the reference origin with $\phi = 0$. For the j^{th} sphere at \vec{r}_j away from O , it scatters a spherical wave with its phase ϕ_j . From direct perspective, ϕ_j would be $2\pi/\lambda$ times the path length difference between waves scattered from the origin and from \vec{r}_j . If the detector is far from the scattering volume, ϕ_j can be expressed as

$$\phi_j = \frac{2\pi}{\lambda} (\overline{AP} + \overline{PB}) = \frac{2\pi}{\lambda} (\hat{k}_i \cdot \vec{r}_j - \hat{k}_f \cdot \vec{r}_j) = (\vec{k}_i - \vec{k}_f) \cdot \vec{r}_j .$$

Recall that we have defined the scattering vector by $\vec{q} \equiv \vec{k}_i - \vec{k}_f$ in subsection 1.2.2.

The above ϕ_j can then be rewritten as

$$\phi_j = \vec{q} \cdot \vec{r}_j . \quad (1.3.6)$$

The total electric field is the sum of the individual field scattered by all particles

$$E(t) = \sum_{j=1}^N E_0 e^{i(\phi_j(t) - \omega_0 t)} , \text{ where } N \text{ is the total number of scatterers. It follows that}$$

the intensity is of the form

$$I(t) = \beta |E(t)|^2 = \beta E_0^2 \sum_j \sum_k e^{i(\phi_j(t) - \phi_k(t))} . \quad (1.3.7)$$

Since all the particles randomly diffuse, \vec{r}_j varies randomly. From Eq. (1.3.6), ϕ_j thus varies randomly, too. Accordingly, $E(t)$ and $I(t)$ become random variables and must be treated in a statistical way. The autocorrelation technique discussed in the former subsections is now serviceable.

The unnormalized autocorrelation function for the intensity $I(t)$ is

$G^{(2)}(\tau) = \langle I(t)^* I(t+\tau) \rangle$. By taking $I(t)$ from Eq. (1.3.7) into $G^{(2)}$, we obtain

$$G^{(2)}(\tau) = \beta^2 E_0^4 \sum_j \sum_k \sum_\ell \sum_m \left\langle e^{-i(\phi_j(t) - \phi_k(t))} e^{i(\phi_\ell(t+\tau) - \phi_m(t+\tau))} \right\rangle . \quad (1.3.8)$$

We must emphasize two important facts about Eq. (1.3.8):

1. The average of the product is the product of the average if terms are statistically independent with each other.
2. $\langle e^{i\phi_j(t)} \rangle = 0$. This is because the particles move about randomly over large distances compared with the wavelength within the averaging time. $\phi(t)$ varies through many cycles of 2π , and since $e^{i\phi} = \cos\phi + i\sin\phi$, both $\cos\phi$ and $\sin\phi$ will vary through many oscillations. The average of $\cos\phi$ and $\sin\phi$ over many oscillations is zero, $\langle e^{i\phi_j(t)} \rangle = 0$ is verified.

The above two facts ensure that any $jk\ell m$ term in Eq. (1.3.8) will be averaged to zero if any one index is different from the other three indices. So, there is only one way to make Eq. (1.3.8) nonzero, that is, pairs of indices are equal. There are three

such cases that will be discussed as follows,

1. $j = k$ and $\ell = m$: assuming that N represent the number of the scatterers, there should be N^2 pairs for this case. When $j = k$ and $\ell = m$, the exponential factor in Eq. (1.3.8) is always unity.

2. $j = \ell$ and $k = m$, but $j \neq k$: there should have $N^2 - N$ pairs for this case, and the exponential factor of each such term becomes

$$S_2 = \left\langle e^{-i(\phi_j(t) - \phi_j(t+\tau))} e^{i(\phi_k(t) - \phi_k(t+\tau))} \right\rangle .$$

3. $j = m$ and $k = \ell$, but $j \neq k$: there should have $N^2 - N$ pairs for this case, and the exponential factor of each such term becomes

$$S_3 = \left\langle e^{-i(\phi_j(t) + \phi_j(t+\tau))} e^{i(\phi_k(t) + \phi_k(t+\tau))} \right\rangle .$$

In case 2 and case 3, S_2 and S_3 can both be rewritten as product of their average.

Since j^{th} and k^{th} particles' motions are statistically independent, we then have

$S_2 = s_2 s_2^*$ and $S_3 = s_3 s_3^*$, where $s_2 = \left\langle e^{-i(\phi(t) - \phi(t+\tau))} \right\rangle$ and $s_3 = \left\langle e^{-i(\phi(t) + \phi(t+\tau))} \right\rangle$. With

the help of Eq. (1.3.6), the above s_2 and s_3 then give $s_2 = \left\langle e^{i\vec{q} \cdot \Delta\vec{r}(t,\tau)} \right\rangle$,

$s_3 = \left\langle e^{-i\vec{q} \cdot (2\vec{r}(t) + \Delta\vec{r}(t,\tau))} \right\rangle \stackrel{\text{fact 1}}{=} \underbrace{\left\langle e^{-i\vec{q} \cdot 2\vec{r}(t)} \right\rangle}_{0, \text{ from fact 2}} \left\langle e^{-i\vec{q} \cdot \Delta\vec{r}(t,\tau)} \right\rangle = 0$, where $\Delta\vec{r}(t,\tau) \equiv \vec{r}(t+\tau) - \vec{r}(t)$.

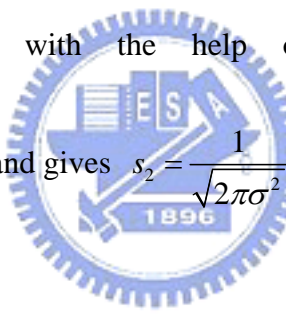
Now, the only remaining question is how we calculate s_2 . For simplicity, let us take

the x-axis along the scattering vector \vec{q} so that $\vec{q} \cdot \Delta\vec{r} = q \cdot \Delta x$. Divide time-axis into

time steps t_0, t_1, \dots spaced equal interval τ apart over the entire averaging time,

and x_0, x_1, \dots are the particle's x -coordinates corresponding to t_0, t_1, \dots , respectively. Since the particles undergo Brownian motion, the values of $\Delta x_j \equiv x_j - x_{j-1}$ will be random variables. They distribute with the probability density $p(\Delta x)$ of a normal random variable mentioned in subsection 1.1.2. We then have

$s_2 = \frac{1}{\sqrt{2\pi\sigma^2}} \int_{-\infty}^{\infty} e^{iq\cdot\Delta x} e^{-(\Delta x)^2/2\sigma^2} d\Delta x$. By employing Euler formula, $e^{iq\cdot\Delta x} = \cos(q\cdot\Delta x) + i\sin(q\cdot\Delta x)$ and taking this expansion into the above s_2 expression, we can simplify the calculation because the sine term is an odd integrand over an even integration interval and therefore vanishes. The remaining cosine term can be easily integrated with the help of Gaussian cosine integral



$$\int_{-\infty}^{\infty} \cos(kx)e^{-ax^2} dx = \sqrt{\frac{\pi}{a}} e^{-\frac{k^2}{4a}}$$

and gives $s_2 = \frac{1}{\sqrt{2\pi\sigma^2}} \int_{-\infty}^{\infty} \cos(q\cdot\Delta x) e^{-(\Delta x)^2/2\sigma^2} d\Delta x = \frac{1}{\sqrt{2\pi\sigma^2}} \sigma \sqrt{2\pi} e^{-\frac{\sigma^2 q^2}{2}} = e^{-\frac{q^2 \sigma^2}{2}}$.

Up to now, we have developed the knowledge needed for writing down an analytic expression for $G^{(2)}$. Recall that the three cases for Eq. (1.3.8), there are N^2 terms each contributing unity and $N^2 - N$ terms each contributing $s_2 s_2^* = e^{-q^2 \sigma^2}$. $G^{(2)}$ is thus of the analytic form

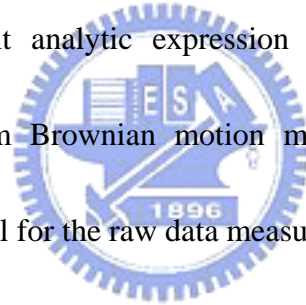
$$G^{(2)}(\tau) = \beta^2 E_0^4 \left[N^2 + (N^2 - N) e^{-q^2 \sigma^2} \right]. \quad (1.3.9)$$

In subsection 1.1.3, we have mentioned that **Einstein** had deduced the mean-square displacement of Brownian particle to be $\langle x^2(t) \rangle = 2D(t - t_0)$. This means the variation of the particle's displacement is proportional to the time interval taken as it

travels in such displacement. So, σ^2 in Eq. (1.3.9) is exactly $\langle x^2(t) \rangle$ and σ^2 is accordingly of the form $\sigma^2 = 2D\tau$. Eq. (1.3.9) can be rewritten as $G^{(2)}(\tau) = \beta^2 E_0^4 \left[N^2 + (N^2 - N) e^{-2Dq^2\tau} \right]$. Thus, we can conclude that the normalized second-order intensity autocorrelation function $g^{(2)}$ shall be a constant plus a decaying exponential just as $G^{(2)}$ is, which yields the form

$$g^{(2)}(\tau) = A + B e^{-\tau/\tau_c} , \quad (1.3.10)$$

where $A \cong 1$ because of the effect of normalization and $\tau_c \equiv \frac{1}{2Dq^2}$ is the characteristic decay time of the autocorrelation function. After a series of derivations, we have derived an explicit analytic expression Eq. (1.3.10) for the intensity autocorrelation function from Brownian motion measurement, and will use this expression as our fitting model for the raw data measured in the test run later on.



In 1851, an English scientist **George G. Stokes** derived an equation for drag force exerted on very small spherical particles in a viscous fluid by solving a condition-limited case of the unsolvable **Navier-Stokes** equation: $\bar{F} = 3\pi d\eta v$, where \bar{F} is frictional force, d is the hydrodynamic diameter of the spherical particle, η is the fluid viscosity, and v is the particle's velocity. This equation implies that the friction constant for this fluid system is

$$\gamma = 3\pi d\eta . \quad (1.3.11)$$

This is the so-called **Stokes'** law. Eq. (1.1.22) told us that $\gamma = \frac{k_B T}{D}$. If we replace the

γ with $3\pi d\eta$ as *Stokes* suggested in Eq. (1.3.11), we shall obtain the well-known

Stokes-Einstein relation

$$D = \frac{k_B T}{3\pi\eta d} . \quad (1.3.12)$$

In Eq. (1.3.10), we have obtained $\tau_c \equiv \frac{1}{2Dq^2}$. By taking D suggested by the

Stokes-Einstein relation and q suggested by Fig. 1-3-4 (b) into τ_c 's denominator

and making appropriate rearrangement, we finally get a serviceable formula that can

be used to determine the hydrodynamic diameter of the solute to be measured in the

following test run,

$$d = \frac{32\pi n^2 k_B T \tau_c \sin^2\left(\frac{\theta}{2}\right)}{3\eta\lambda_0^2} , \quad (1.3.13)$$

where λ_0 is the incident wavelength in vacuum and n is solution's index of refraction.

12-*nm* diameter Au nanoparticles were used for the test samples of this study.

The experimental setup is sketched in Fig. 1-3-5.

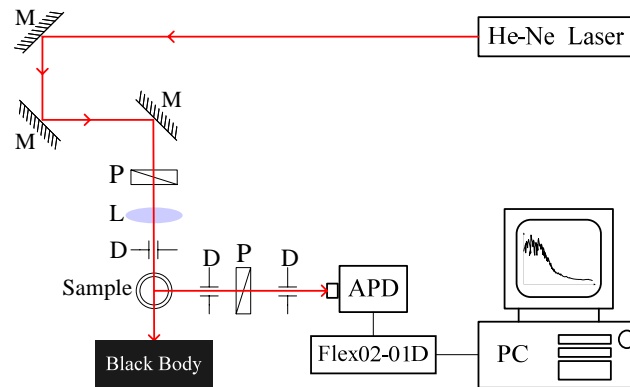
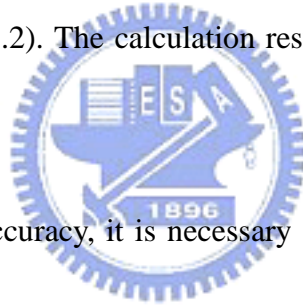


Fig. 1-3-5 Schematic experimental setup for determining particle size in the sample solution. M:mirror ; P:polarizer ; L:lens ; D:diaphragm.

A series of different concentration solutions with solutes being the Au nanoparticles were tested. We used a He-Ne laser of 632.8 *nm* wavelength with an output power of 15 *mW* as our light source. The laser was focused onto the sample by a lens. After passing through the sample, the strong forward unscattered light was directed into a homemade beam dump. A silicon avalanche photodiode (Si APD) was used to detect the scattered light at 90° scattering angle. The detected photons were converted into photoelectron pulses, and these pulses were fed into the Flex02-01D digital correlator to calculate $g^{(2)}$ via Eq. (1.3.2). The calculation result was shown on PC's monitor in real time.



To obtain satisfactory accuracy, it is necessary to average the correlator output over a long enough time; generally to attain a statistical uncertainty of 1 % requires a measurement over 10,000 characteristic decay times of the autocorrelation function [11]. In our test run, the solute particles with known diameter can suggest how long the measuring time should be in order to reach the desired statistical uncertainty less than 1%. From Eq. (1.3.13), by taking d to be 12 *nm* and the other parameters taking proper values (will be given later), τ_c is approximated in the order of 10^{-4} sec.. This estimated value suggests that we shall use a measuring time at least $10000 \times 10^{-4} = 1$ sec. in order to reach a statistical uncertainty that is lower than 1%.

In the following test run, the measuring times were all set to be 180 sec., thus leads to a statistically uncertainty that is much lower than 1%.

Our samples were Au nanoparticles dissolved in a variety of deionized water/ethylene glycol (E.G.) mixture by varying the concentrations of ethylene glycol (E.G.) in water. Six different weight percent of E.G. in water were prepared: 0% , 20% , 40% , 60% , 80% , 100% . The higher the E.G. concentration is, the more viscous the solution exhibits. Fig. 1-3-6 shows the raw data (open symbols) of the measured $g^{(2)}$ in the case of concentration 100% ethylene glycol solution in which 12-*nm* Au nanoparticles suspend and the fitting result (the solid red-color curve).

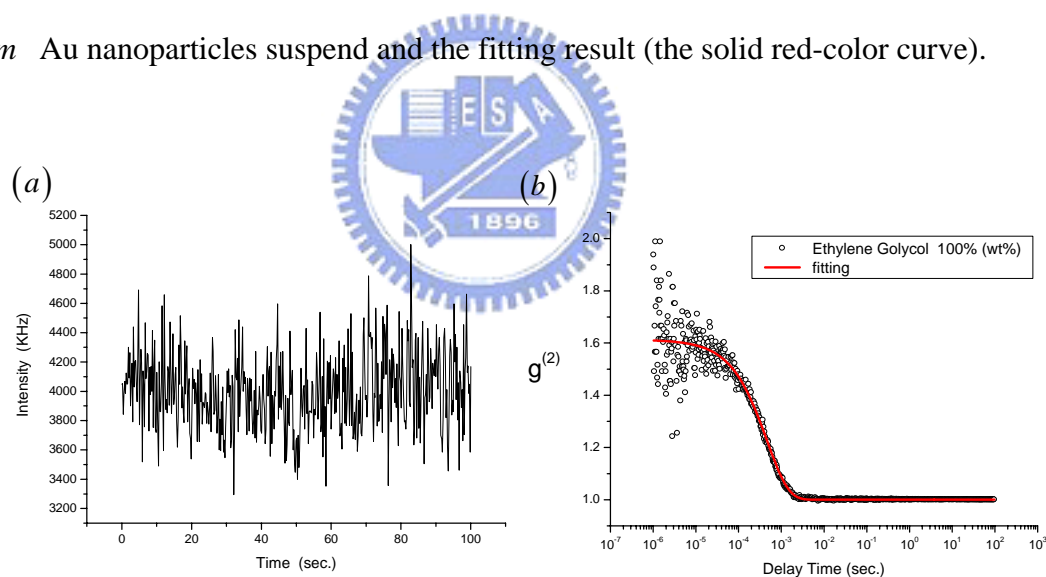


Fig. 1-3-6 (a) The intensity (kilo-photocounts per second) trace recorded the scattering light intensity scattered from 100% (wt%) ethylene glycol solution in which 12-*nm* Au nanoparticles suspended; **(b)** the autocorrelation function calculated from the intensity information in **(a)**.

Eq. (1.3.10) suggests that $g^{(2)}(\tau) = A + Be^{-\tau/\tau_c}$ can be used as the fitting model for the autocorrelation function from solution with monodisperse Brownian particles.

However, there are in fact no perfect monodisperse Brownian particles. There must be distributive in particle's size, making particles appear polydisperse. This implies that we should make some modifications on Eq. (1.3.10) in order to achieve better fitting quality. The modification strategy we adopted is introducing a stretching parameter s to the decaying exponential part, so as to get a more flexible fitting model shown below

$$g^{(2)}(\tau) = A + B \exp[-(\tau/\tau_c)^s] . \quad (1.3.14)$$

The effect of small deviations from central τ_c is incorporated into the stretching parameter s , in other words, s can serve as an equalizer that equalizes the effect of polydisperse system and the effect of monodisperse system plus s itself. Thereafter, we shall use Eq. (1.3.14) to fit the raw data measured by Flex02-01D digital correlator, and then obtain the useful fitting parameter τ_c to determine the solute particle's hydrodynamic diameter via Eq. (1.3.13). Take the case in Fig. 1-3-6 as an example, the nanoparticle's hydrodynamic diameter in such a solution is calculated in such a way

$$\begin{aligned} d_{100\%} &= \frac{32\pi n^2 k_B T \tau_c}{3\eta \lambda_0^2} \sin^2\left(\frac{\theta}{2}\right) \\ &= \frac{32\pi (1.4308)^2 (1.38 \times 10^{-23}) (301 \text{ K}) (46.527 \times 10^{-5} \pm 3.6292 \times 10^{-5} \text{ s})}{3(0.015367 \text{ Pa} \cdot \text{s}) (632.8 \times 10^{-9} \text{ m})^2} \sin^2\left(\frac{90^\circ}{2}\right) \\ &\cong 10.773 (\pm 0.840) \text{ nm} , \end{aligned}$$

where the related parameters and the corresponding units are shown during the

process of calculation. By the same token, the nanoparticle's hydrodynamic diameters corresponding to the solutions with different viscosities can be derived in the same way, the results and the related parameters are given below,

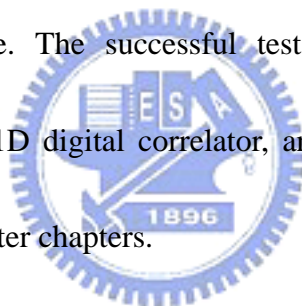
Parameter E.G. wt %	n	η (Pa · s)	τ_c (10^{-5} s)	diameter (nm)
0 %	1.3306	0.000836	6.5543 (\pm 0.6827)	24.125 (\pm 2.513)
20 %	1.3507	0.001313	8.4518 (\pm 1.3922)	20.411 (\pm 3.362)
40 %	1.3707	0.002156	12.163 (\pm 1.4132)	18.422 (\pm 2.140)
60 %	1.3907	0.003823	21.309 (\pm 1.8196)	18.736 (\pm 1.600)
80 %	1.4108	0.007274	30.575 (\pm 2.7496)	14.541 (\pm 1.308)
100 %	1.4308	0.015367	46.527 (\pm 3.6292)	10.773 (\pm 0.840)

Table 1-3-1 The 12 nm nanoparticle's hydrodynamic diameters correspond to various viscous solutions; E.G. wt% means ethylene glycol's percentage of the water solvent; n represents index of refraction; η represents viscosity of solution; τ_c represents characteristic decay time of the autocorrelation function.

It is not contradictory that nanoparticle appears to have different hydrodynamic diameter in different viscous solutions since it possesses different *Debye length* in different viscous solutions. *Debye length* is defined as the thickness of the electric double layer that surrounds the nanoparticle. Pure water produces a larger double layer around a nanoparticle because of its ultra-low ionic strength, and this larger

double layer reduces the diffusion speed of the nanoparticle and then results in a larger apparent hydrodynamic diameter. The more ethylene glycol are added to the water solvent, the higher ionic strength the solvent behaves; and the higher ionic strength the solvent behaves, the thinner double layer the nanoparticle possesses, this leads to the smaller apparent hydrodynamic diameter. This trend clearly appears in Table 1-3-1.

Our Flex02-01D digital correlator can give us quite accurate answers given in Table 1-3-1 and has the capability of telling such a subtle hydrodynamic diameter differences at the *nm* scale. The successful test run guarantees the excellent performance of the Flex02-01D digital correlator, and we shall use it to probe the other physical system in the later chapters.



Chapter 2. Probing the Twist Anchoring Strength of Liquid Crystal Molecules on Various Alignment Surfaces

2.1 Overview of Liquid Crystals Phases

Generally speaking, matters can exhibit three physical states, *solid*, *liquid*, and *gaseous* phases. These three states of matter can be classified according to their degrees of spatial order. The molecular constituents in a solid material not only occupy specific spatial positions, but they also orient in a specific spatial direction. This is because there are large attractive forces holding these molecules in place, even though they might be allowed to vibrate. The situation in liquid state is quite different in that the molecules of this state neither occupy specific average positions nor orient in a specific direction. These molecules are free to diffuse about in a random fashion and constantly change their orientations. The degree of order in a liquid is therefore much less than that in a solid. Attractive forces still exist in a liquid, but they are much weaker than forces in a solid because the intermolecular distances in a liquid are larger than those in a solid. In gaseous state, the most freely and chaotically molecular motion makes the intermolecular distances much larger than those in liquid state, and thus causes the attractive forces in between are much less than those in liquid state. The degree of order in gaseous state is therefore the least one among all states of

matter [12, 13, 14].

In late 19th century, scientists found that there exists a number of mesophases that possess a degree of order intermediate between those of the conventional liquid and solid states. The molecules in these mesophases retain somewhat orientational order, but lack most of their positional order. These mesophases are named *liquid crystals* (LCs) since they preserve a combination of properties that are commonly associated with both liquids (fluidity) and crystals (anisotropy).

LCs consist of several subphases categorized by their spatial arrangement. The main theme of this thesis work will focus on the two among them: *nematic* and *smectic* phases. Let us take an elongated molecular system as our example. Elongated molecules bump into each other less when they tend to point in the same average direction, a fact that acts to stabilize aligned phases. This preferred average direction is called the *director* of the LC, and is denoted by \hat{n} . In nematic phase, the molecules are positionally random just as in liquid phase, whereas they are orientationally correlated, they point in the direction of \hat{n} . Generally, nematic molecules are centrosymmetric and optically uniaxial since their physical properties in the two mutually orthogonal directions perpendicular to the director are physically equivalent. As to smectic phase, not only do the molecules in this phase possess small amount of orientational order, but there is also a small amount of positional order. These

molecules are free to bounce around randomly, but they tend to point along the director and arrange themselves in layers. The schematic representations are shown in

Fig. 2-1-1.

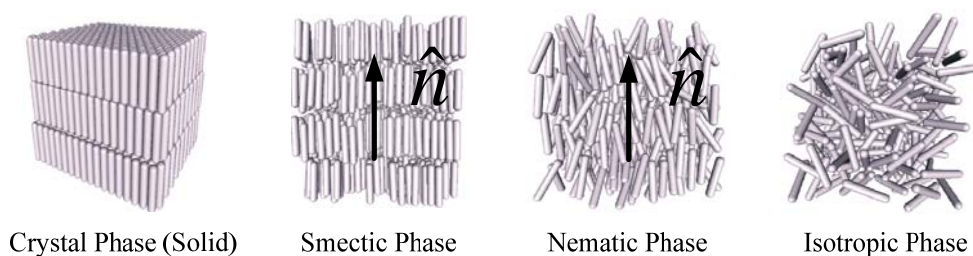


Fig. 2-1-1 Spatial arrangements of elongated molecules in various phases. Smectic and nematic phases belong to liquid crystalline phase : \hat{n} means their directors [6].

2.2 Theoretical Background of Molecular Fluctuations in Liquid

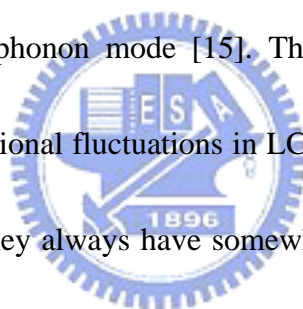
Crystals

2.2.1 Broken Symmetry and Elementary Excitations

The concepts of *symmetry* and *broken symmetry* are similar in solid crystals and more general condensed-phase materials. In solid crystals, a given crystalline configuration belongs to one of the 230 space groups [15]. These groups all possess positional and translational order of constituent atoms or ions. In condensed matter, taking LCs as an example, they could be either positionally disordered or orientationally disordered. Here, the concept of orientational order can be roughly explained by the degree of the molecular orientations' tendency toward the same direction. With these concepts in mind, we can proceed with the discussion of the

comparison between the phenomena of the positional order in solid crystals and the orientational order in LCs.

Another useful concept in describing the constituent elements' behavior is *collective excitations*. This term describes phenomena that a large number of constituents act coherently and cooperatively. In solid crystals, one of these collective excitations is *phonon*, which is a collective behavior and represents oscillations of crystal lattices as a whole. Each constituent of the lattices cooperates in this collective motion coherently with its neighbors, which implies the same oscillating frequency of all constituents for a given phonon mode [15]. The analogy to phonons in solid crystals are molecular orientational fluctuations in LCs. Molecules in LCs are usually positionally disordered, but they always have somewhat orientational order and their orientations fluctuate coherently over fairly long distances. The collective excitations in solid crystals (phonons) are usually *underdamped*, whereas the collective excitations in LCs (molecular orientational fluctuations) are always *overdamped*. The oscillatory behaviors of phonons result from their positionally ordered configurations that would reduce the probability of bumping into each other, so they are relatively free to oscillate. However, in LCs the inertial forces are much smaller than the viscous force, a result originating from the positional disorder of the spatial configurations of LC constituents and the relation between the molecular fluctuations and their energy



dissipations as mentioned in Chapter 1.

Let us introduce the dispersion relations for phonons in solid crystals and orientational fluctuations in nematic LCs to gain further insight into their comparison.

The dispersion relations are illustrated in the schematic diagram of Fig. 2-2-1.

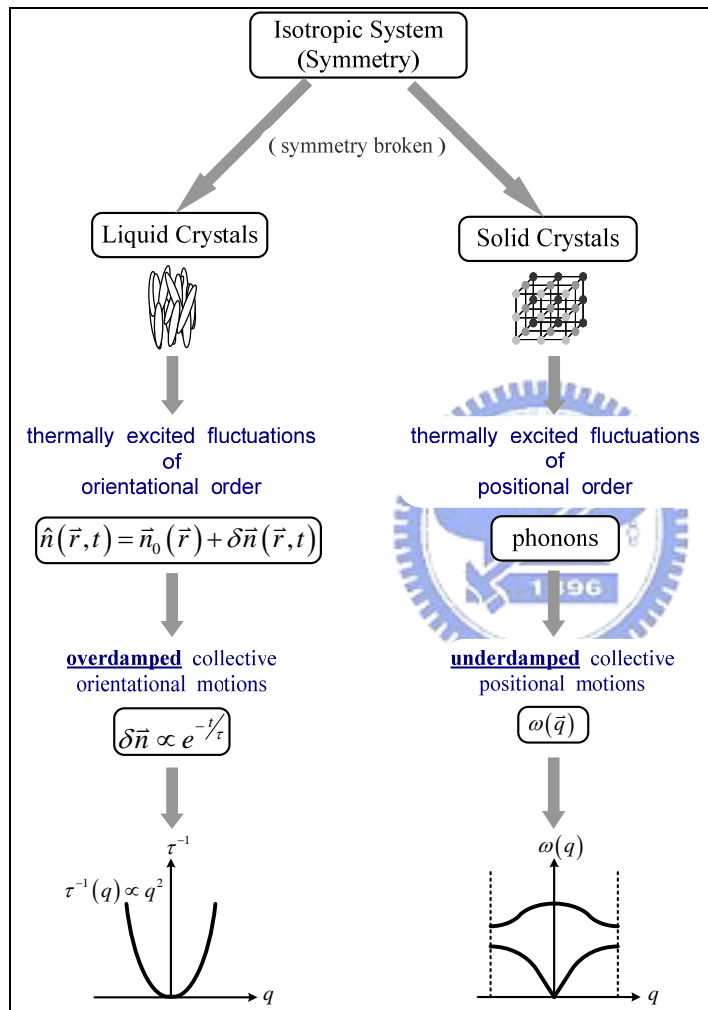


Fig. 2-2-1 The comparison of positional order in solids crystals and orientational order in nematic liquid crystals; the bottom two figures are their corresponding dispersion relations. Note that they both show the presence of zero-frequency modes; \vec{q} is wavevector of fluctuation, \bar{n}_0 is the average orientation of the director, $\delta\vec{n}$ is the fluctuation of the director, τ is the relaxation time of $\delta\vec{n}$, $\omega(q)$ is the oscillating frequency of the phonons [15].

Some similarities and differences of the dispersion relations between liquid crystals and solid crystals could be found. From the figure, there both exist zero-frequency mode. In solid crystals, the long-wavelength limit of acoustic phonon modes always

leads to zero-frequency mode. In nematic LCs, the long-wavelength limit of molecular orientational fluctuations also leads to zero-frequency mode. However, their q -dependent behavior are quite different. The acoustic phonon in solids shows linear dispersion: $\omega \propto q$, whereas the dispersion relation in nematic LCs is parabolic: $\tau^{-1} \propto q^2$, which is a characteristic feature of overdamped systems.

The existence of zero-frequency modes is closely related to the spontaneous breaking of the continuous symmetry in a system. Their relation is unveiled in the context of *Goldstone theorem*: if the ground state of a nonrelativistic many-body system is one with broken continuous symmetry, a gapless branch of collective excitations of this system exists and tries to restore the lost symmetry. The term “gapless” means that in the limit of zero q , the frequency (or the relaxation rate) of collective excitations also approaches zero, which are shown in the bottom two illustrations in Fig. 2-2-1.

It is this zero-frequency (long-wavelength) mode that makes all the neighboring atoms in solid crystals move coherently and all the neighboring molecules in LCs rotate coherently when external perturbations are exerted on them. These phenomena are depicted in the following figure.

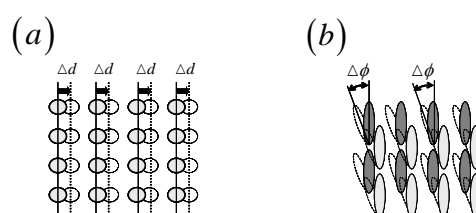


Fig. 2-2-2 (a) coherent collective excitations in solid crystals; **(b)** coherent collective excitations in liquid crystals.

The coherent nature of collective excitations in matter can be fully explained by the existence of this zero-frequency *Goldstone* mode, and this concept will be of great help for our later discussion.

2.2.2 Orientational Fluctuations in Thin Nematic Liquid Crystal Cells

The long-wavelength fluctuations of the optical axes of molecules in nematic LCs give rise to light scattering because of the existence of dielectric constant fluctuations due to the molecular anisotropy, which is illustrated in Eq. (1.2.13); and further, since these thermally-induced orientational fluctuations are not static, the scattering light flickers. The dynamics of these fluctuations is thus revealed in this flicker phenomenon. To probe this phenomenon with our dynamic light scattering apparatus described in Chapter 1, we must prepare nematic LC cells with the director of LC pointing along the *easy axis*, which can be defined to the direction of surface treatment in advance. There are several surface treatment methods for producing aligning layers for LC devices nowadays, and we shall discuss them in the later content.

When LC materials deform with external perturbations, three types of

deformation occur, they are *splay*, *twist*, and *bend*, whose schematic representations are sketched below,

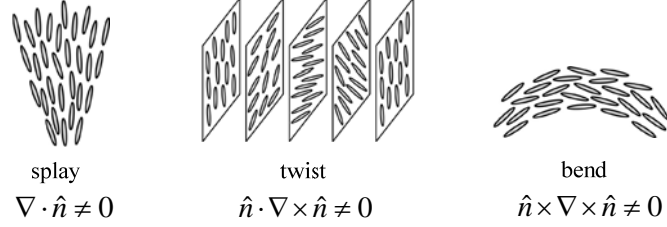


Fig. 2-2-3 The three types of deformation in nematics. \hat{n} represents their director [6].

In mechanical point of view, mechanical internal energy inside a physical system varies when the system suffers mechanical deformation. Hence, the deformed LC exhibits a distortion energy density that shall be expressed in terms of the three types of mechanical deformation

$$E_d = \frac{1}{2} K_1 (\nabla \cdot \hat{n})^2 + \frac{1}{2} K_2 (\hat{n} \cdot \nabla \times \hat{n})^2 + \frac{1}{2} K_3 (\hat{n} \times \nabla \times \hat{n})^2, \quad (2.2.1)$$

where $K_i (i=1,2,3)$ are **Frank** elastic constants associated with the three types of deformation: K_1 corresponds to splay with $\nabla \cdot \hat{n} \neq 0$; K_2 corresponds to twist with $\hat{n} \cdot \nabla \times \hat{n} \neq 0$; and K_3 corresponds to bend with $\hat{n} \times \nabla \times \hat{n} \neq 0$. The unit of $K_i (i=1,2,3)$ is energy per length, and thus the unit of E_d is energy per cubic length.

For nematic LCs in a cell, their director \hat{n} always suffers small fluctuation $\delta \vec{n}$ from its average orientation \vec{n}_0 . The small fluctuation $\delta \vec{n} = \hat{n} - \vec{n}_0$ will relax to zero in a certain time [14]. For simplicity, we choose \vec{n}_0 along \hat{z} and decompose $\delta \vec{n}$

in two spatially independent directions \hat{x} and \hat{y} to give

$$\hat{n}(\vec{r}, t) = \bar{n}_0(\vec{r}) + \delta\bar{n}(\vec{r}, t) = \hat{z} + n_x(\vec{r}, t)\hat{x} + n_y(\vec{r}, t)\hat{y} . \quad (2.2.2)$$

Taking $\hat{n}(\vec{r}, t)$ of Eq. (2.2.2) into Eq. (2.2.1), the distortion energy reduces to

$$E_d = \frac{1}{2} \int \left\{ K_1 \left(\frac{\partial n_x}{\partial x} + \frac{\partial n_y}{\partial y} \right)^2 + K_2 \left(\frac{\partial n_x}{\partial x} - \frac{\partial n_y}{\partial y} \right)^2 + K_3 \left[\left(\frac{\partial n_x}{\partial z} \right)^2 + \left(\frac{\partial n_y}{\partial z} \right)^2 \right] \right\} d\vec{r} . \quad (2.2.3)$$

Moreover, in order to retrieve useful information from the dispersion relation mentioned in subsection 2.2.1, we appeal to the language used in wave vector space.

We first *Fourier* transform $n_x(\vec{r})$ and $n_y(\vec{r})$ into $n_x(\vec{q})$ and $n_y(\vec{q})$ with $n_j(\vec{r}) = \sum_{\vec{q}} n_j(\vec{q}) e^{i\vec{q}\cdot\vec{r}}$, $j = x, y$. By substituting the above transforms into Eq. (2.2.3),

the total distortion free energy becomes

$$E = \int E_d d^3\vec{r} = \frac{V}{2} \sum_{\vec{q}} \left\{ K_1 |n_x(\vec{q})q_x + n_y(\vec{q})q_y|^2 + K_2 |n_x(\vec{q})q_y - n_y(\vec{q})q_x|^2 + K_3 [|n_x(\vec{q})|^2 + |n_y(\vec{q})|^2] q_z^2 \right\} , \quad (2.2.4)$$

where V is the sample volume. It is convenient to diagonalize the quadratic form in

Eq. (2.2.4) by a linear transformation: $\delta\bar{n}(\vec{q}) = n_x(\vec{q})\hat{x} + n_y(\vec{q})\hat{y} \rightarrow$

$\delta\bar{n}(\vec{q}) = n_1(\vec{q})\hat{e}_1 + n_2(\vec{q})\hat{e}_2$ for any given \vec{q} , where the unit vector \hat{e}_2 is normal to \vec{q}

and \bar{n}_0 , and \hat{e}_1 is normal to \hat{e}_2 and \bar{n}_0 . The new coordinates system is shown in

Fig. 2-2-4.

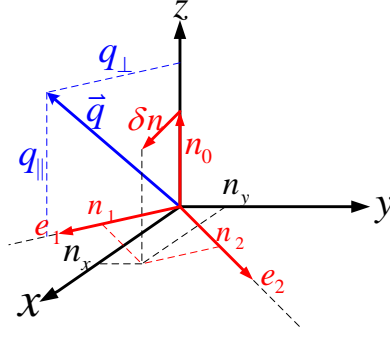


Fig. 2-2-4 Definition of the new coordinates system in LC.

In this new coordinates system, the total distortion free energy has a simple diagonal form

$$E = \frac{V}{2} \sum_{\vec{q}} \left[\left(K_1 q_{\perp}^2 + K_3 q_{\parallel}^2 \right) \cdot |n_1(\vec{q})|^2 + \left(K_2 q_{\perp}^2 + K_3 q_{\parallel}^2 \right) \cdot |n_2(\vec{q})|^2 \right], \quad (2.2.5)$$

where $q_{\parallel} = q_z$ and $q_{\perp} = \vec{q} \cdot \hat{e}_1$. Eq. (2.2.5) indicates that $n_1(\vec{q})$ describes a distortion that is a mixture of splay and bend, and $n_2(\vec{q})$ depicts a distortion that is a mixture of twist and bend. The classical *equipartition theorem* tells us that the average energy per degree of freedom of a system in thermal equilibrium is equal to $\frac{1}{2} k_B T$. That is $\left\langle \frac{V}{2} (K_1 q_{\perp}^2 + K_3 q_{\parallel}^2) \cdot |n_1(\vec{q})|^2 \right\rangle = \frac{1}{2} k_B T$ and $\left\langle \frac{V}{2} (K_2 q_{\perp}^2 + K_3 q_{\parallel}^2) \cdot |n_2(\vec{q})|^2 \right\rangle = \frac{1}{2} k_B T$, where $\langle \rangle$ denotes taking thermal average. After some algebraic rearrangements, the above two formulae become

$$\left\langle |n_1(\vec{q})|^2 \right\rangle = \frac{k_B T}{V (K_1 q_{\perp}^2 + K_3 q_{\parallel}^2)}, \quad \left\langle |n_2(\vec{q})|^2 \right\rangle = \frac{k_B T}{V (K_2 q_{\perp}^2 + K_3 q_{\parallel}^2)}. \quad (2.2.6)$$

French physicist *de Gennes* came up with a notion of *molecular field* for LC [14].

From the distortion energy density per small fluctuating deviation $\delta \vec{n}$ shown in Eq.

(2.2.6), we can define a molecular field as

$$h_\alpha = -\left(K_\alpha q_\perp^2 + K_3 q_\parallel^2\right) n_\alpha \quad \alpha = 1, 2 \quad . \quad (2.2.7)$$

In *Onsager's* viewpoint, a fluctuation shall experience a restoring “force” , that is the molecular field h_α . Therefore, $\left(K_\alpha q_\perp^2 + K_3 q_\parallel^2\right)$ can be viewed as the corresponding force constant. Furthermore, for a fluctuating system showing viscous overdamped behavior, the relaxation dynamics shall have the form

$$\frac{\partial}{\partial t} n_\alpha(\vec{q}) = -\frac{1}{\tau_\alpha(\vec{q})} n_\alpha(\vec{q}) \quad , \quad (2.2.8)$$

where $\tau_\alpha(\vec{q})$ is the relaxation time of this overdamped system. By intuition, the

relaxation rate $\frac{1}{\tau_\alpha(\vec{q})}$ in Eq. (2.2.8) must be proportional to the restoring force

constant $\left(K_\alpha q_\perp^2 + K_3 q_\parallel^2\right)$,

$$\frac{1}{\tau_\alpha(\vec{q})} = \frac{K_\alpha q_\perp^2 + K_3 q_\parallel^2}{\eta_\alpha(\vec{q})} \quad , \quad (2.2.9)$$

where $\eta_\alpha(\vec{q})$ is the proportional constant and known as the effective viscosity of the system.

Recall that we have let $\hat{n}(\vec{r}, t) = \vec{n}_0(\vec{r}) + \delta\vec{n}(\vec{r}, t) = \hat{z} + n_x(\vec{r}, t)\hat{x} + n_y(\vec{r}, t)\hat{y}$ in Eq. (2.2.2). In the following derivation, we shall assume that $n_x(\vec{r}, t)$ represents the twist deviation and $n_y(\vec{r}, t)$ represents the deviation in LC tilt direction. Substituting this $\hat{n}(\vec{r}, t)$ into the hydrodynamic equation for the director field

$\eta \frac{\partial \hat{n}}{\partial t} = K \nabla^2 \hat{n} - K(\hat{n} \cdot \nabla^2 \hat{n})\hat{n}$ [16]. Here, η is the viscosity mentioned in Eq. (2.2.9) and

K denotes the effective elastic constant, $K = K_1 = K_2 = K_3$, under the *one-constant*

approximation suggested by *de Gennes* [14]. We then have

$$\left. \begin{aligned} \eta \frac{\partial n_x}{\partial t} &= K \nabla^2 n_x \\ \eta \frac{\partial n_y}{\partial t} &= K \nabla^2 n_y \end{aligned} \right\} \Rightarrow \eta \frac{\partial (\delta \vec{n})}{\partial t} = K \nabla^2 (\delta \vec{n}) , \quad (2.2.10)$$

and the corresponding boundary conditions at $y=0$ and $y=d$ can be expressed as

$$\left\{ \begin{aligned} -K \frac{\partial n_x}{\partial y} \Big|_{y=0} + W_1 n_x \Big|_{y=0} &= 0 , & K \frac{\partial n_x}{\partial y} \Big|_{y=d} + W_2 n_x \Big|_{y=d} &= 0 , \\ -K \frac{\partial n_y}{\partial y} \Big|_{y=0} + W_1 n_y \Big|_{y=0} &= 0 , & K \frac{\partial n_y}{\partial y} \Big|_{y=d} + W_2 n_y \Big|_{y=d} &= 0 . \end{aligned} \right.$$

Here W_1 and W_2 are the *anchoring energy coefficients* with unit being energy per square length of the substrates at $y=0$ and $y=d$, respectively. These boundary

conditions are determined by a torque balance condition from the bulk elastic deformations and the surface torque acting on the LC at the boundaries [17].

Obtaining anchoring energy coefficients is the main theme in this chapter. Note that the hydrodynamic equation as well as the boundary conditions are the same for both

fluctuation modes, so we expect to see the same results from both twist and tilt modes.

Therefore, we are going to discuss the twist fluctuation mode $n_x(\vec{r}, t)$ only. The

hydrodynamic equation $\eta \frac{\partial n_x}{\partial t} = K \nabla^2 n_x$ in Eq. (2.2.10) is a standard diffusion

equation, whose general solution is $n_x(\vec{r}, t) = [\alpha \cos(q_y \cdot y) + \beta \sin(q_y \cdot y)] e^{i(q_x x + q_z z)} e^{-t/\tau}$

with the relaxation time $\tau = \frac{\eta}{Kq^2}$. The mathematical form of τ has already been

given in Eq. (2.2.9) under one-constant approximation of *Frank* elastic formalism of

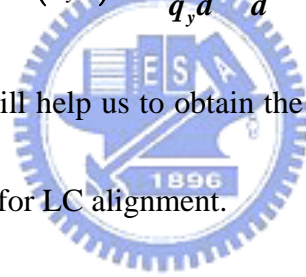
LC material. The boundary conditions for the twist fluctuation can now be expressed

$$\text{as } \begin{cases} W_1\alpha - Kq_y\beta = 0 , \\ [W_2 \cos(q_y d) - Kq_y \sin(q_y d)]\alpha + [W_2 \sin(q_y d) + Kq_y \cos(q_y d)]\beta = 0 . \end{cases}$$

The system of homogeneous linear equations for α and β has a nontrivial solution if its coefficient determinant equals zero, which leads to $\frac{\lambda_1 + \lambda_2}{d} \cot(q_y d) = -\frac{1}{q_y d} + \frac{\lambda_1 \lambda_2}{d^2} q_y d$, where λ_1 and λ_2 are the extrapolation lengths defined as $\lambda_i = \frac{K}{W_i}$ ($i=1,2$). If we treat the aligning layers on the two substrates of a LC cell with the same condition, their anchoring coefficients shall be the same, that is, $W_1 = W_2 = W$. Thus, the above eigenvalue equation reduces to

$$\frac{2\lambda}{d} \cot(q_y d) = -\frac{1}{q_y d} + \frac{\lambda^2}{d^2} q_y d \quad (2.2.11)$$

with $\lambda = \frac{K}{W}$. This formula will help us to obtain the anchoring coefficient of certain specifically treated substrates for LC alignment.



2.3 The Relationship of the Anchoring Energy Strength with Autocorrelation Time and Its Measurement with Dynamic Light Scattering

In chapter 1, we have introduced the autocorrelation technique for describing a fluctuation process. At that time, we took it for granted that the correlation time (characteristic decay time) is equal to the relaxation time of the fluctuation dynamics.

Here, to be more accurate, we explicitly define the correlation time τ_c to be

$$\tau_c \equiv \int_0^{\infty} \frac{\langle Y(0)Y(\tau) \rangle - \langle Y \rangle^2}{\langle Y^2 \rangle - \langle Y \rangle^2} d\tau . \quad (2.3.1)$$

Here Y can be any given physical process [5]. This formula can be further illustrated with the following sketch.

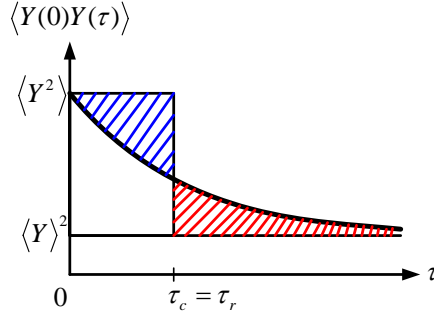
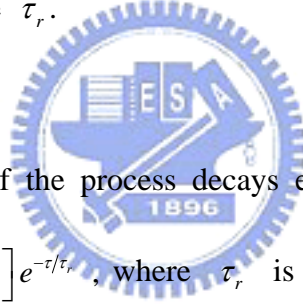


Fig. 2-3-1 τ_c is the τ -position at which the two sections (blue & red) are equal in area; in the case of exponentially decaying fluctuation, τ_c is equal to its relaxation time τ_r .



If the fluctuating behavior of the process decays exponentially with the form of

$\langle Y(0)Y(\tau) \rangle - \langle Y \rangle^2 = [\langle Y^2 \rangle - \langle Y \rangle^2] e^{-\tau/\tau_r}$, where τ_r is the relaxation time of this

fluctuating process, Eq. (2.3.1) becomes $\tau_c \equiv \int_0^{\infty} \frac{\langle Y(0)Y(\tau) \rangle - \langle Y \rangle^2}{\langle Y^2 \rangle - \langle Y \rangle^2} d\tau = \int_0^{\infty} e^{-\tau/\tau_r} d\tau = \tau_r$.

This result suggests that we can get the τ_r of the dynamical process simply by measuring τ_c of its corresponding correlation function under the condition of the process decaying exponentially [5, 18, 21]. The orientational fluctuations in nematic LC cells happen to be the case.

Recall that, in the derivation process of Eq. (1.3.10), we did not place any restriction on the shape of the scatterer. This implies that the pure fluctuation mode

(for example, pure twist mode) of LC molecules in a cell also inherits the character of exponential decay. Hence, in the following discussion, we shall treat τ_c and τ_r as the same symbol τ to take into account their identical nature in this case.

We are now in a position to derive the relationship between the correlation time τ and the anchoring energy coefficient W . To simplify our discussion, we divide the anchoring effect into three regimes: *infinitely strong*, *strong but finite*, *weak* anchorings.

1. Infinitely Strong Anchoring: Let us review the secular equation

$$\frac{2\lambda}{d} \cot(q_y d) = -\frac{1}{q_y d} + \frac{\lambda^2}{d^2} q_y d \quad (2.2.11)$$

with $\lambda = \frac{K}{W}$. In this infinitely strong anchoring case ($W \rightarrow \infty$), $\lambda \rightarrow 0$.

The secular equation becomes: $\cot(q_y d) = -\frac{1}{2\lambda q_y} + \frac{\lambda}{2} q_y \rightarrow -\infty$.

This implies $\sin(q_y d) = 0$, which leads to

$$q_{yn} = (n+1) \frac{\pi}{d} \quad n = 0, 1, 2, \dots$$

Under the condition of pure twist fluctuation mode, Eq. (2.2.9) yields a

simple relation $\frac{1}{\tau} = \frac{Kq^2}{\eta}$, and by substituting the fundamental mode

($n=0$) of q_{yn} into this simple relation, we then obtain the correlation

time — sample thickness relationship

$$\tau = \frac{\eta}{Kq_{y0}^2} = \frac{\eta}{K \left(\frac{\pi}{d} \right)^2} = \frac{\eta}{K} \frac{d^2}{\pi^2}.$$

2. Strong but Finite Anchoring: The discussion in infinitely strong

anchoring regime tells us the fundamental fluctuation mode is $q_{y_0} = \frac{\pi}{d}$.

This is incorrect when the anchoring is not infinite. In this case, we use an

appropriate approximation for $q_{y_0}d = \pi - x$, where x represents a small

deviation from π . By taking this into account, the secular equation Eq.

(2.2.11) becomes

$$\begin{aligned}
\frac{2\lambda}{d} \cot(\pi - x) &= -\frac{1}{\pi - x} + \frac{\lambda^2}{d^2}(\pi - x) \approx -\frac{1}{\pi - x} \quad \text{since } \lambda \ll d \\
\Rightarrow -\frac{2\lambda}{d} \cot(x) &= -\frac{1}{\pi - x} \\
\Rightarrow \frac{2\lambda}{d} \left(\frac{1}{x} - \frac{x}{3} - \frac{x^3}{45} + \dots \right) &= \frac{1}{\pi - x} \\
\Rightarrow \frac{2\lambda}{dx} &\approx \frac{1}{\pi - x} \\
\Rightarrow x &= \frac{2\lambda\pi}{d + 2\lambda} \\
\Rightarrow q_{y_0}d = \pi - x &= \pi - \frac{2\lambda\pi}{d + 2\lambda} = \frac{\pi d}{d + 2\lambda} \\
\Rightarrow q_{y_0} &= \frac{\pi}{d + 2\lambda} .
\end{aligned}$$

Having obtained the fundamental mode q_{y_0} for strong but finite

anchoring regime, we substitute q_{y_0} into $\frac{1}{\tau} = \frac{Kq^2}{\eta}$ to yield

$$\begin{aligned}
\tau &= \frac{\eta}{Kq_{y_0}^2} = \frac{\eta}{K \left(\frac{\pi}{d + 2\lambda} \right)^2} = \frac{\eta}{K} \frac{(d^2 + 4d\lambda + 4\lambda^2)}{\pi^2} \\
&= \frac{\eta}{K} \frac{d^2 \left(1 + \frac{4\lambda}{d} + \frac{4\lambda^2}{d^2} \right)}{\pi^2} \approx \frac{\eta}{K} \frac{d^2}{\pi^2} \left(1 + \frac{4\lambda}{d} \right) \quad \text{since } \lambda \ll d . \quad (2.3.2)
\end{aligned}$$

3. Weak Anchoring: In the weak anchoring regime ($W \rightarrow 0$), $\lambda \rightarrow \infty$, the

secular equation becomes $\cot(q_y d) = -\frac{1}{2\lambda q_y} + \frac{\lambda}{2} q_y \rightarrow \infty$. This

suggests to use $q_{y0} d = x$ for the fundamental mode in the weak

anchoring case. Substituting $q_{y0} d = x$ into the secular equation Eq.

(2.2.11), we obtain

$$\begin{aligned}
\frac{2\lambda}{d} \cot(x) &= -\frac{1}{x} + \frac{\lambda^2}{d^2} x \\
\Rightarrow \frac{2\lambda}{d} \left(\frac{1}{x} - \frac{x}{3} - \frac{x^3}{45} + \dots \right) &= -\frac{1}{x} + \frac{\lambda^2}{d^2} x \\
\Rightarrow \frac{2\lambda}{d} \left(\frac{1}{x} - \frac{x}{3} \right) &\approx -\frac{1}{x} + \frac{\lambda^2}{d^2} x \quad \Rightarrow \frac{2\lambda}{d} \left(1 - \frac{x^2}{3} \right) = -1 + \frac{\lambda^2}{d^2} x^2 \\
\Rightarrow x^2 = \frac{6\lambda d + 3d^2}{3\lambda^2 + 2\lambda d} = q_{y0}^2 d^2 &\quad \Rightarrow q_{y0}^2 = \frac{6\lambda + 3d}{d(3\lambda^2 + 2\lambda d)} \\
\Rightarrow \tau = \frac{\eta}{K q_{y0}^2} = \frac{\eta}{K} \frac{d(3\lambda^2 + 2\lambda d)}{6\lambda + 3d} &= \frac{\eta d}{W} \frac{3\lambda + 2d}{6\lambda + 3d} = \frac{\eta d}{W} \frac{3\lambda}{6\lambda} \left(1 + \frac{2d}{3\lambda} \right) \\
&= \frac{\eta d}{2W} \left(1 + \frac{2d}{3\lambda} \right) \left(1 - \frac{d}{2\lambda} \right) = \frac{\eta d}{2W} \left(1 + \frac{2d}{3\lambda} - \frac{d}{2\lambda} - \frac{d^2}{3\lambda^2} \right) \\
&\approx \frac{\eta}{2W} d \left(1 + \frac{d}{6\lambda} \right) \quad \text{since } \lambda \gg d . \tag{2.3.3}
\end{aligned}$$

2.4 The Twist Anchoring Strength of Nematic Liquid Crystal

Molecules on Various Alignment Surfaces

In section 2.3, we have derived the relationship between the correlation time and

the anchoring energy coefficient of the LC's molecular fluctuations in a nematic cell.

We measured the correlation times of some practical homemade nematic LC cells with different surface treatments in order to understand the correlation between the magnitude of the anchoring strength and the corresponding surface treatment techniques.

Three different surface treatment conditions were prepared for our dynamic light scattering study. They are *strong mechanical rubbing* alignment, *photoalignment* with special photoactive polyimide (*RN1349* from *Nissan Chemical Ltd.*), and *photoalignment* with a composite layer system of *RN1349* and *LCP (liquid crystal polymer)*.



For the strong mechanical rubbing alignment, we used a roller coated with a velvet cloth to rub the polyimide on a glass substrate. The LC molecules deposited on it can be strongly aligned in a preferred direction (easy axis). This kind of alignment technique produces very stable and strong surface anchoring quality [19, 20, 21]. In contrast to rubbing alignment, photoalignment technique provides a clean and non-contact surface treatment. We illuminated the photoalignment film deposited on a glass substrate with linearly polarized UV light, the photoactive polyimide changes its configuration, which induces an easy axis pointing in the direction perpendicular to the polarization of the UV light [19, 22, 23, 24]. As the recent developments show, this non-contact alignment technology seems to be promising for applications in the

display industry because the contact-induced sample contamination is prevented.

2.4.1 Experimental Setup and Considerations

The LC used in our experiment was *4-n-pentyl-4'-cyanobiphenyl* (5CB), whose nematic range is $22\text{ }^{\circ}\text{C} - 35\text{ }^{\circ}\text{C}$. The experiment was performed at constant ambient temperature of $25\text{ }^{\circ}\text{C}$. All the three cells were in homogeneous configuration with the easy axes on both substrates being antiparallel. In addition, since what we were interested in was their surface anchoring effect, these cells were all made directly contact (no spacers in between) to diminish the LC's bulk effect. The cell gaps used were all $d \doteq 1\text{ }(\mu\text{m})$, which were approximated by the polarimetry measurements. Our experimental setup is sketched in Fig. 2-4-1.

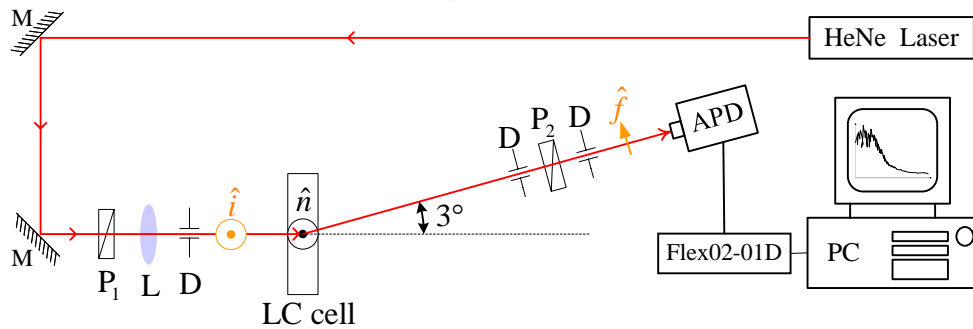


Fig. 2-4-1 Experimental setup for measuring the anchoring energy coefficients. M: mirror ; P_1 & P_2 : polarizers ; L: lens ; D: diaphragm ; the polarization of the incoming beam \hat{i} is parallel to the LC's director \hat{n} , but perpendicular to the outgoing beam's polarization \hat{f} and the scattering plane. The scattering angle was chosen small, 3° in this experiment, so as to minimize the contribution of splay / bend fluctuations.

Note that the polarizers P_1 and P_2 must be in cross-polarized so that the P_2 -directional component of scattered light coming from the scattering region is permitted to pass through P_2 , which flicker in response to the LC's molecular fluctuations.

The knowledge of the molecular twist fluctuations in a nematic cell developed in the former sections help us determine the azimuthal anchoring energy coefficients of the cells. In Fig. 2-4-1, the scattering vector $\vec{q} \equiv \vec{k}_i - \vec{k}_f$ was perpendicular to the LC's director \hat{n} so that the q_{\parallel} in Fig. 2-2-4 vanished, together with the use of a small scattering angle. These pre-cautions allow us to probe the pure twist component of the fluctuations, as illustrated in the following figure.

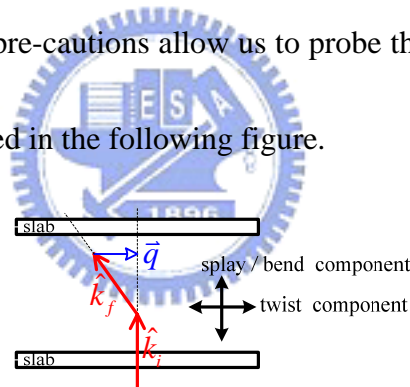


Fig. 2-4-2 The scattering angle was so small that the scattering vector \vec{q} was almost parallel to the substrates, which made it possible to probe the pure twist component of the fluctuations.

To understand why an experimental arrangement with small scattering angle is needed for unambiguously probing the twist component of the LC's molecular fluctuations, let us first review some concepts of the scattering theory mentioned in chapter 1.

Consider the specific case in which the element $\delta\varepsilon_{if}(\vec{r}, t)$ of the dielectric

fluctuation tensor in Eq. (1.2.13) is a simple sinusoidal wave of frequency ω traveling in a direction \vec{k} , and has the form $\delta\varepsilon_{if}(\vec{r}, t) = \delta\varepsilon_0 e^{j(\vec{k}\cdot\vec{r}-\omega t)}$, where $\delta\varepsilon_0$ is its amplitude. Taking this equation into Eq. (1.2.13) yields

$$E_s(\vec{r}, t) = \frac{k_f^2 E_0 \delta\varepsilon_0}{4\pi\varepsilon_0 r} e^{i(\vec{k}_f \cdot \vec{r} - \omega_f t)} \int_{V'} d^3 r' e^{i\vec{q} \cdot \vec{r}'} e^{i(\vec{k} \cdot \vec{r}' - \omega t)} = \frac{k_f^2 E_0 \delta\varepsilon_0}{4\pi\varepsilon_0 r} e^{i\vec{k}_f \cdot \vec{r}} \int_{V'} d^3 r' e^{i(\vec{q} \cdot \vec{r}' - \omega_f t)} e^{i(\vec{k} \cdot \vec{r}' - \omega t)} .$$

The above equation tells us we cannot calculate it directly in complex form, instead, we should return it to its sinusoidal form as follows

$$\begin{aligned} \tilde{E}_s(\vec{r}, t) &= \frac{k_f^2 E_0 \delta\varepsilon_0}{4\pi\varepsilon_0 r} \operatorname{Re} \left[e^{i\vec{k}_f \cdot \vec{r}} \right] \int_{V'} d^3 r' \operatorname{Re} \left[e^{i(\vec{q} \cdot \vec{r}' - \omega_f t)} \right] \cdot \operatorname{Re} \left[e^{j(\vec{k} \cdot \vec{r}' - \omega t)} \right] \\ &= \frac{k_f^2 E_0 \delta\varepsilon_0}{4\pi\varepsilon_0 r} \underbrace{\operatorname{Re} \left[e^{i\vec{k}_f \cdot \vec{r}} \right]}_A \int_{V'} d^3 r' \cos(\vec{q} \cdot \vec{r}' - \omega_f t) \cdot \cos(\vec{k} \cdot \vec{r}' - \omega t) \\ &= \frac{A}{2} \int_{V'} d^3 r' \left\{ \cos \left[(\vec{q} + \vec{k}) \cdot \vec{r}' - (\omega_f + \omega) t \right] + \cos \left[(\vec{q} - \vec{k}) \cdot \vec{r}' - (\omega_f - \omega) t \right] \right\} . \end{aligned}$$

The scattered field in complex form thus gives

$$\begin{aligned} E_s(\vec{r}, t) &= \frac{k_f^2 E_0 \delta\varepsilon_0}{8\pi\varepsilon_0 r} e^{i\vec{k}_f \cdot \vec{r}} \int_{V'} d^3 r' \left\{ e^{i[(\vec{q} + \vec{k}) \cdot \vec{r}' - (\omega_f + \omega) t]} + e^{i[(\vec{q} - \vec{k}) \cdot \vec{r}' - (\omega_f - \omega) t]} \right\} \\ &= \frac{k_f^2 E_0 \delta\varepsilon_0}{8\pi\varepsilon_0 r} e^{i\vec{k}_f \cdot \vec{r}} \left\{ e^{-i(\omega_f + \omega) t} \int_{V'} d^3 r' e^{i(\vec{q} + \vec{k}) \cdot \vec{r}'} + e^{-i(\omega_f - \omega) t} \int_{V'} d^3 r' e^{i(\vec{q} - \vec{k}) \cdot \vec{r}'} \right\} . \quad (2.4.1) \end{aligned}$$

From **Fourier transform** formula $\int_{-\infty}^{\infty} e^{-i\omega t} dt = 2\pi\delta(\omega)$, $E_s(\vec{r}, t)$ can be found to reach its maximum when the two integrals $\int_{V'} d^3 r' e^{i(\vec{q} + \vec{k}) \cdot \vec{r}'}$ and $\int_{V'} d^3 r' e^{i(\vec{q} - \vec{k}) \cdot \vec{r}'}$ in Eq. (2.4.1) are sharply peaked at $\vec{q} \pm \vec{k} = 0$, viz $\vec{k} = \pm\vec{q}$. That is, the *differential scattering cross section* (the intensity of the scattered light per solid angle, which is proportional to E_s^2) is the largest when $\vec{k} = \pm\vec{q}$. To be more explicit, the dielectric

fluctuation $\delta\varepsilon$ may fluctuate in very many directions. However, only those fluctuations in $\pm\vec{q}$ directions will largely contribute to the scattered light. This result gives us a hint that we should choose small scattering angle to make the scattering vector be nearly parallel to the direction of twist fluctuation. In our case, the direction was parallel to both the scattering plane and the cell's substrates as shown in Fig. 2-4-2. By doing so, the scattered light will almost come from the contribution of the twist component of the whole fluctuations, and from the former discussion we know that the dynamics of this twist part fluctuation highly correlates to the cell's azimuthal anchoring strength.



2.4.2 Experimental Results and Discussion

The measured results are shown below with an order of a LC cell with *strong mechanical rubbing*, a *photoalignment* cell with photoactive polyimide *RN1349* (from *Nissan Chemical Ltd.*), and a *photoalignment* cell with composite layers of *RN1349* and *LCP (liquid crystal polymer)*. The results were taken at one specific position on each cell.

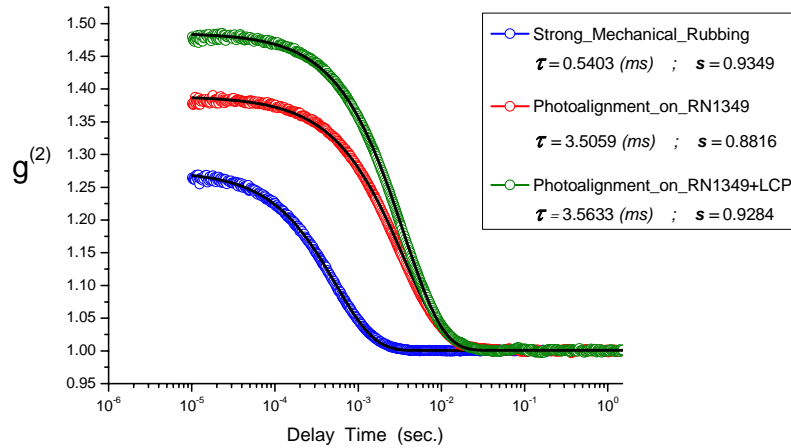
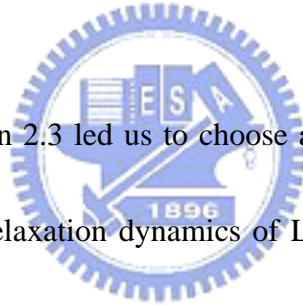


Fig. 2-4-3 The colorful circle lines are the measured raw data, and the black solid lines are their corresponding fitting results. The fitting model is the stretched exponential function $g^{(2)}(t) = A + B \exp\left[-(t/\tau)^s\right]$. τ is the correlation time and s is the stretching parameter.

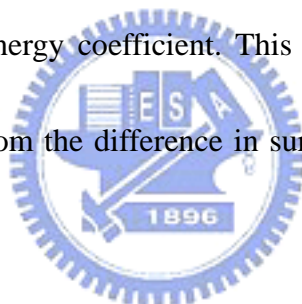


The discussion in section 2.3 led us to choose a stretched exponential function as the fitting model for the relaxation dynamics of LC's molecular fluctuations in a cell. The fitting parameter τ represents the correlation time of the relaxation dynamics; the fitting parameter s can be used as a measure to reveal how close the dynamics approaches a single fluctuation mode. If the fluctuating dynamics is exactly a single fluctuation mode without any mode-mixing, s shall be equal to unity.

As shown in Fig. 2-4-3, the fitting parameters are $\tau = 0.5403 \text{ ms}$ and $s = 0.9349$ for the strong mechanical rubbing cell; $\tau = 3.5059 \text{ ms}$ and $s = 0.8816$ for the photoalignment cell with RN1349; $\tau = 3.5633 \text{ ms}$ and $s = 0.9284$ for the photoalignment cell with composite layers of RN1349 and LCP.

From these fitting data, we can easily observe the differences among them. Firstly, the correlation time for the strong mechanical rubbing cell is less than those for the photoalignment cells by about one order of magnitude. Secondly, as to the photoalignment cells, the value taken by s seems to depend on whether LCP was deposited on RN1349 layer or not. Let us examine these two major differences with more caution.

We begin the discussion by examining the difference of the correlation time. In section 2.3, we achieved a conclusion that the correlation time is highly correlated with the surface anchoring energy coefficient. This hints that the difference of the correlation time may come from the difference in surface anchoring strengths of LC cells.



Having derived the $\tau-W$ relationships in section 2.3, we can use these relationships to determine the anchoring energy coefficient W of each cell. According to many reports published in literature, surface rubbing treatment usually generates rather strong surface anchoring strength, whereas the UV-induced alignment shows weak anchoring strength. We therefore expect that our strong mechanical rubbing cell is strong anchoring and our photoalignment cells are weak anchoring. We then retrieve the corresponding anchoring energy coefficients from the measured data to see whether these retrieved values are in accord with the expected results.

From Eq. (2.3.2)

$$\tau = \frac{\eta d^2}{K \pi^2} \left(1 + \frac{4\lambda}{d} \right) \quad \text{for } \lambda \ll d , \quad (2.3.2)$$

by substituting all the parameters of the rubbing cell with known values into the equation $0.5403 \times 10^{-3} = \frac{50 \times 10^{-3}}{1 \times 10^{-11}} \frac{(1 \times 10^{-6})^2}{\pi^2} \left(1 + \frac{4 \times 10^{-11}}{1 \times 10^{-6} \times W} \right)$, we achieved a value of

$W_{\text{rubbing}} \doteq 6.014 \times 10^{-4} \text{ (J/m}^2\text{)}$. Here, the effective *Frank* elastic constant $K \doteq 1 \times 10^{-11} \text{ (N)}$ and the rotational viscosity $\eta \doteq 50 \text{ (mPa}\cdot\text{s)}$ at $T = 25 \text{ }^\circ\text{C}$ [25].

For the photoalignment cells, we adopt the following approximative formula

$$\tau = \frac{\eta}{2W} d \left(1 + \frac{d}{6\lambda} \right) \quad \text{for } \lambda \gg d . \quad (2.3.3)$$

Similarly, by substituting all the parameters of the photoalignment cells with known values into Eq. (2.3.3), it yields $\tau = \frac{50 \times 10^{-3}}{2W} \times 10^{-6} \left(1 + \frac{W \times 10^{-6}}{6 \times 10^{-11}} \right) = 3.5059 \times 10^{-3}$

$\Rightarrow W_{\text{photo.}} \doteq 8.093 \times 10^{-6} \text{ (J/m}^2\text{)}$; and $\tau = \frac{50 \times 10^{-3}}{2W} \times 10^{-6} \left(1 + \frac{W \times 10^{-6}}{6 \times 10^{-11}} \right) = 3.5633 \times 10^{-3}$

$\Rightarrow W_{\text{photo.+LCP}} \doteq 7.945 \times 10^{-6} \text{ (J/m}^2\text{)}$.

Having derived all the three cells' anchoring energy coefficients, let us check these results to see whether they are reasonable or not. We expected high anchoring strength from the strong mechanical rubbing cell and our measured anchoring coefficient is $W_{\text{rubbing}} \doteq 6.014 \times 10^{-4} \text{ (J/m}^2\text{)}$. We expected that the photoalignment cells are weak anchoring and our measured values are: $W_{\text{photo.}} \doteq 8.093 \times 10^{-6} \text{ (J/m}^2\text{)}$ and $W_{\text{photo.+LCP}} \doteq 7.945 \times 10^{-6} \text{ (J/m}^2\text{)}$. The results agree well with our expectation, and thus we confidently conclude that the mechanically rubbing-induced anchoring

strength is much larger than that from photoalignment mechanism by about two orders of magnitude.

Let us examine the schematic shown below to intuitively illustrate the inverse tendency between τ and W .

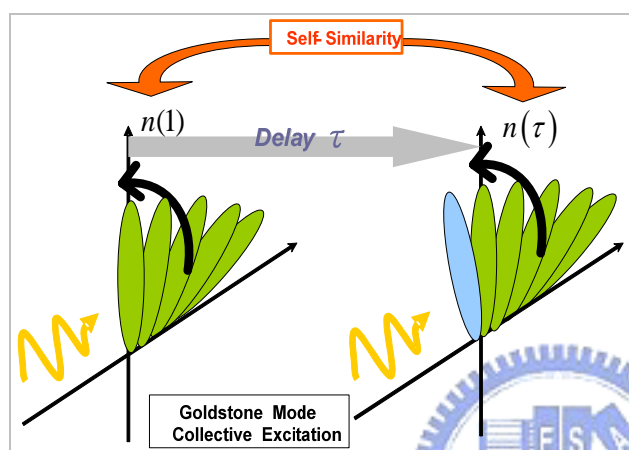


Fig. 2-4-4 The self-similarity existing in the collective excitation of LC *Goldstone* mode: Yellow wave represents the incident light field. $n(1)$ is the photoelectron pulses counted at initial time, and $n(\tau)$ is the photocounts at a delay τ from the initial time.

As shown in the figure, photocounts $n(\tau)$ at a delay τ will be very close to the initial photocounts $n(1)$, provided that the delay τ is very small. This is because what the incident light field sees are the almost identical geometric configurations due to the “collective” excitation nature of LC. In other words, after the delay τ , the collective excitation of LC molecules just produces a small rotation, the incident light field shall therefore see very similar geometric configuration except for the LC molecule marked by blue color shown in Fig. 2-4-4. Seeing a similar geometric configuration implies that the transmitted light fields will be also very alike. Therefore, $n(\tau)$ must be very close to $n(1)$, and this is the origin of the

self-similarity in photocounts. Once the self-similarity is confirmed, the principle of the **Schwartz's** inequality discussed in subsection 1.3.1 assures a high correlation value.

How about the decay behavior? The explanation could also be found with this picture. As the delay time τ becomes larger, the collective excitation of LC molecules generates a much larger rotation. At this stage, the incident light field experiences a configuration less similar to that in the initial time. This leads to a smaller degree of similarity between $n(1)$ and $n(\tau)$ and a lower correlation value.

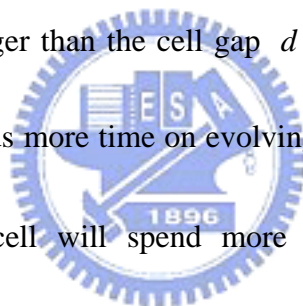
The larger the delay time τ is, the smaller the correlation value will be.

We can extend these intuitive pictures to yield a connection with the LC cell's surface anchoring strength. We have understood that the high correlation values result from the similar configurations the incident light field experiences. As time goes by, the transient LC configuration is less and less similar to the initial one. But how fast does the LC configuration changes from the most similar one to the least similar one?

To answer this question, we need a reference to compare with! Since the excitations in LC cells are collective, the effective wavelength λ_E of the standing wave induced by the collective excitation in a confined cell can be used to reveal the changing rate of LC configuration. When λ_E is large, the LC spends more time to change from the most similar configuration to the least similar one. Whereas when λ_E is small, it

takes the LC configuration less time to evolve. The comparison must be taken under the same physical conditions, that is, the same viscosity, the same ambient temperature, *etc.*

Let us consider two limiting cases: infinitely strong anchoring cell and weak anchoring cell. In the infinitely strong anchoring cell, the two substrates anchor the contacting LC molecules tightly, so these two contact surfaces play roles as nodal points of the standing wave. The effective λ_E is thus equal to the cell gap d . In the weak anchoring cell, the two substrates anchor the contacting LC molecules loosely, the effective λ_E could be larger than the cell gap d . Since we have shown that for longer λ_E LC medium spends more time on evolving their configuration. This leads to that a weak anchoring cell will spend more time to change its molecular configuration. The concept of the “more time” implies “larger correlation time” because it is this time that reflects correctly the rate of LC configuration changing from high to low correlation. Hence, we reach the point that a weak anchoring cell exhibits a characteristic long correlation time in its scattered optical signal; Similar analysis on an infinitely strong anchoring cell reveals that a strong anchoring cell shall possess a small correlation time in its scattered optical signal. Two illustrating schematic diagrams are shown below to facilitate our interpretation.



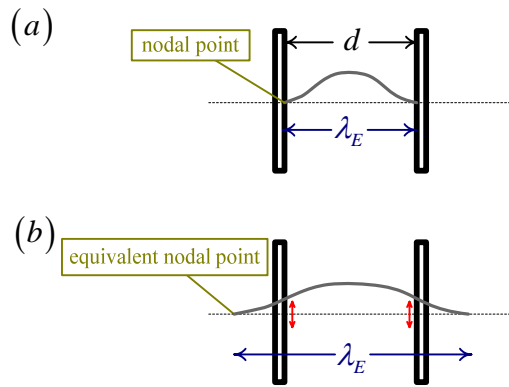


Fig. 2-4-5 (a) Effective λ_E of the collective excitation-induced standing wave in the strong anchoring cell; (b) effective λ_E of the collective excitation-induced standing wave in the weak anchoring cell.

Up to now, we have only examined the difference in correlation time among cells with different surface treatment. Next we shall study the difference in the stretching parameter s . In the beginning, we have mentioned that s can be used as a measure of how close the fluctuation approaches a purely single exponential dynamics. The s obtained from the two photoalignment cells are different. It appears that the cell with LCP has a purer fluctuation dynamics than that one without LCP. We are interested to know about what role LCP plays in the photoalignment process.

A LCP is a polymer produced by binding mesogenic molecules together. In our experiment, the LCP we used was *1,4-phenylene-bis{4-[6-(acryloyloxy)-hexyloxy]benzoate}*, whose structural formula is depicted in Fig. 2-4-6 (a) below.

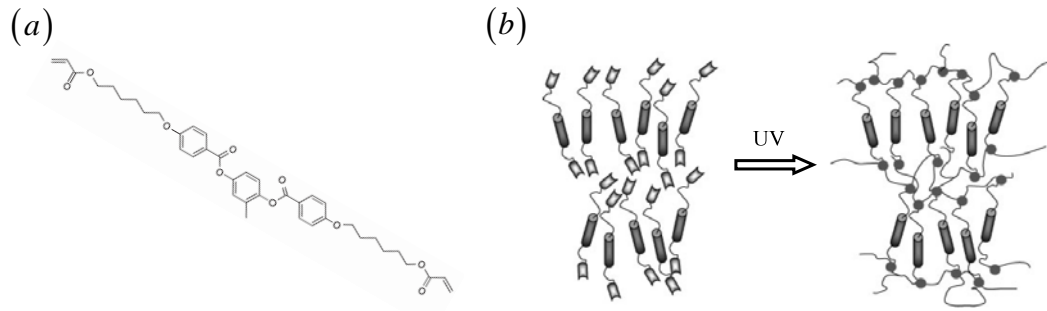


Fig. 2-4-6 (a) The structural formula of the LCP used in our experiment ; (b) the morphological change of the LCP in the *photopolymerization* process.

The LCP was deposited on the top of the LPUV-defined photo-alignment layer of the cell. After illuminated by UV light, the polymerizable mesogenic groups in the photo-alignment layer were crosslinked to yield a small degree of uniaxial alignment.

This effect of inducing macroscopic alignment of LCP followed the *photopolymerization* process, improves the aligning quality of LC molecules in a LC device [22, 23, 24]. The LC molecules contacting with the LCP surfaces thus possessed a higher order of orientation, and the corresponding orientation fluctuation mode was purer, which was supported by the observation that higher value of stretching parameter s was obtained for the photoalignment cell with composite layers of RN1349 and LCP.

To evaluate the possibility of our data in fact resulting from probing into the singularities or defects in the cell, we measured 50 more positions on each cell. The total experimental results are summarized in the following two histograms.

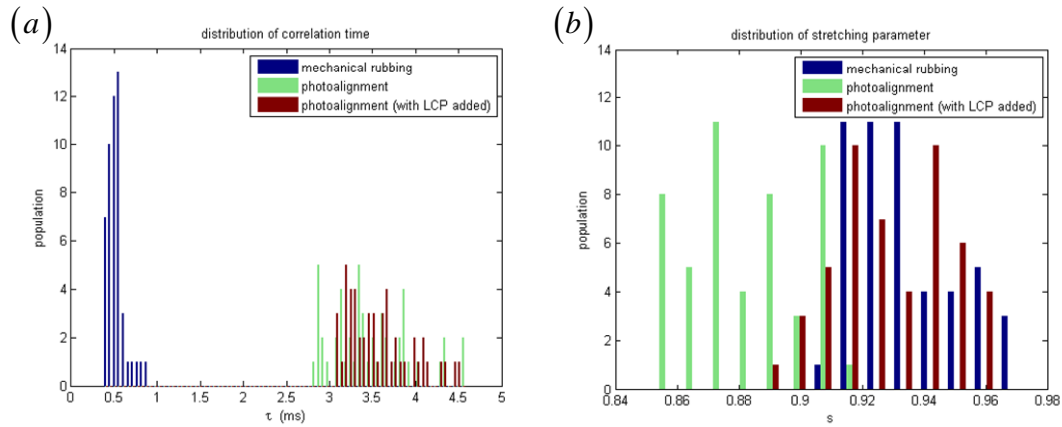


Fig. 2-4-7 (a) Distribution of correlation times of the three cells with different surface treatments. 50 points were probed for each cell. The abscissa is correlation time and the ordinate is its corresponding population; **(b)** distribution of stretching parameters of the three cells with different surface treatments. 50 points were probed for each cell. The abscissa is stretching parameter and the ordinate is its corresponding population.

From Fig. 2-4-7 (a), we can see that the mechanical rubbing cell does have smaller correlation times than those of photoalignment cells, this is in agreement with the fact that mechanical rubbing produces stronger anchoring strength than that produced by photoaligning method. We can deduce that the photoalignment cells have similar anchoring strength no matter whether LCP is deposited or not. However, from Fig. 2-4-7 (b), we find that LCP does play a role in improving the alignment order of LC molecules in the cell. By adding LCP layer, the stretching parameter s was improved to the level as that reached by the mechanical rubbing method.

Chapter 3. Probing the Thermal Fluctuation in the Conic Motion of Surface-Stabilized Ferroelectric Liquid Crystals

3.1 Introduction to the Physics of SSFLC

3.1.1 Basic Concepts of Ferroelectric Liquid Crystals

In section 2.1, we have seen that the liquid crystal phase may have different subphases. One special kind of them is the smectic phase that possess a small amount of positional order, which leads to a molecular structure arranged in layers. The two types of the smectic phase liquid crystals shown in Fig. 3-1-1 (a) and (b) differ in their molecular orientations. The director in the *smectic A* phase is in the direction of the layer normal while the director in the *smectic C* phase is at an angle smaller than 90° from the layer normal [26, 27].

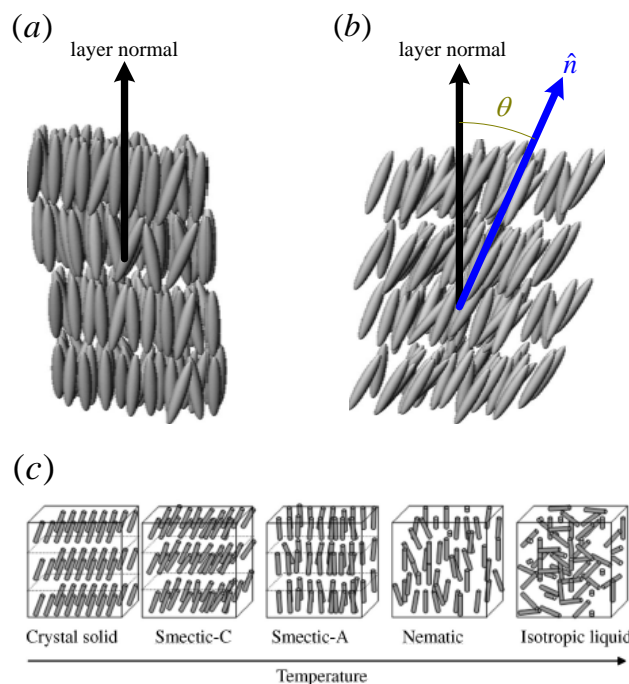


Fig. 3-1-1 (a) Smectic A phase; **(b)** smectic C phase, where θ is the tilt angle and \hat{n} is the director of the LC [26]. **(c)** For thermotropic matter, different phase corresponds to different temperature range. The Smectic C phase exists in the lower temperature range than the smectic A phase does [27].

In describing some physical properties in condensed matter physics regime, it is usually necessary to look into the symmetry structure possessed by a specific matter phase. If a structure remains unchanged after translated in any direction by any distance, it possesses the translational symmetry. Likewise, if it remains unchanged after rotated about any axis by any angle, reflected from any plane that is oriented in any direction, or inverted through any point, this structure possesses rotation symmetry, reflection symmetry, or inversion symmetry respectively [28]. Take the isotropic liquid phase in Fig. 3-1-1 (c) as an example, it can be translated, rotated, reflected, and inverted in any way such that its structure looks exactly the same. An isotropic liquid phase thus possesses a high degree of symmetry in that it possesses almost all the symmetry. When the temperature is cooled down to the nematic phase range, this phase with somewhat orientational order still possesses all the possible translational, reflection, and inversion symmetries, however, only those 180° -rotations about axes perpendicular to the director are left to contribute to the small amount of rotation symmetries. In other words, some rotation symmetries are broken when the isotropic liquid phase undergoes the phase transition to the nematic

phase. Similarly, the phase transitions from nematic to smectic A, smectic A to smectic C, and smectic C to solid crystal all suffer symmetry broken. Knowing the basic concepts of symmetry is helpful to an understanding of ferroelectricity in LCs.

In crystallography, structures that contain an inversion center as one of its symmetry elements are called *centrosymmetric* structures. In non-centrosymmetric structures, there often exists a phenomenon that a net displacement of charges is induced due to their non-inversional constituent arrangement. It is this net displacement of charges that produces an equivalent electric polarization. This result hints that ferroelectric materials must possess non-centrosymmetric configurations.

As to liquid crystals, how can they become ferroelectric? In 1975, **Robert B. Meyer** gave the answer [28]. He predicted that tilted, layered liquid crystal phases of *chiral* molecules must be ferroelectric. The term “chiral” means the property of not possessing inversion symmetry. From **Meyer’s** prediction, the smectic C phase may be a promising candidate.

As shown in Fig. 3-1-1 (b), the smectic C phase is centrosymmetric since it possesses inversion symmetry. To become ferroelectric, replacing the original molecules with chiral molecules is a feasible way and it really does by virtue of the solid evidence from the practical experiments. The first ferroelectric liquid crystal molecule was synthesized by organic chemists with a structure similar to molecules

that could form smectic C liquid crystal phase. But to produce spontaneous polarization that a ferroelectric material should possess, an asymmetric carbon atom should exist near one end of the molecule. The asymmetric carbon atom that serves as the chiral part of the whole molecule represents a carbon atom bound to four different atoms in order to induce inversion symmetry broken. The structural formula and the temperature ranges correspond to different phases of this molecule are shown below.

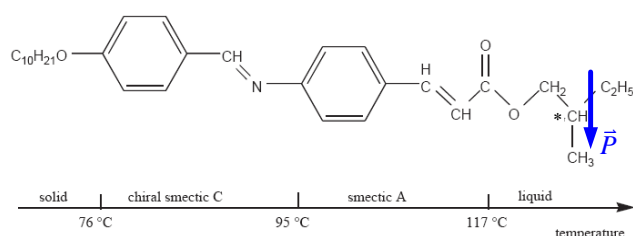


Fig. 3-1-2 The first ferroelectric liquid crystal molecule DOBAMBC. The carbon atom marked by an asterisk (*) is referred to as an asymmetric one. \vec{P} represents the spontaneous polarization of the molecule [28].

A chiral smectic C (SmC^*) phase LC also has layered structure as well as a typical smectic phase LC does, but its director traverses to outline a cone as it rotates around the layer normal from layer to layer with a typical helical pitch of a few microns. A molecule in SmC^* always possesses a spontaneous polarization \vec{P} (Fig. 3-1-2) that tends to orient parallel to the layer and rotates as the director rotates around the cone, which is shown in the following figure.

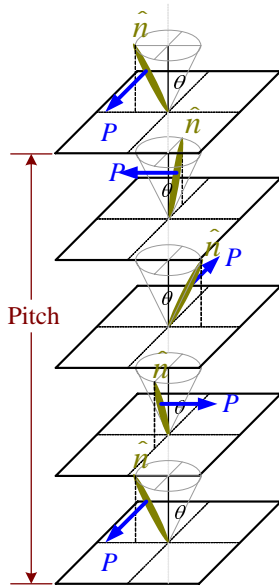


Fig. Fig. 3-1-3 The layered structure of SmC^* . The chiral molecule with specific spontaneous polarization rotates around the layer normal to outline a cone from layer to layer with a typical helical pitch of a few microns. The director \hat{n} makes the same angle θ with the layer normal. \vec{P} represents its induced electric polarization.

3.1.2 Optical Properties of SSFLC

Although each ferroelectric LC molecule has its own spontaneous polarization just like that shown in Fig. 3-1-2, Fig. 3-1-3 tells us that there is no net electric polarization in a bulk sample because of the overall cancellation of the polarizations in each layer. However, we can use external fields to induce a net electric polarization existing in the ferroelectric material. This implies that we may have a chance to utilize this electrical property for certain applications. *Surface-stabilized ferroelectric liquid crystal (SSFLC)* device is one of them.

With the knowledge of SmC^* discussed in subsection 3.1.1 in mind, the molecules in SmC^* phase undergo conic motions unceasingly, but this behavior is not what we want in electro-optical applications that usually require unidirectionally oriented directors [27]. *Clark and Lagerwall* came up with a smart idea for

overcoming this problem. Their brilliant invention was a SSFLC device in bookshelf structure that is shown in Fig. 3-1-4.

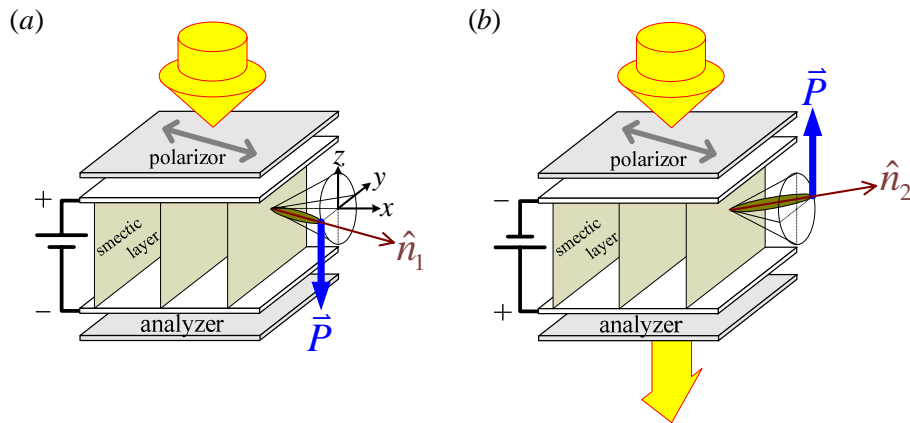
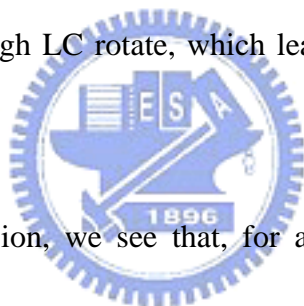


Fig. 3-1-4 Two bistable states of a bookshelf type SSFLC device. The polarity of the external applied electric field switches the device on either (a) dark state or (b) bright state.

The ferroelectric LC is filled into the space between two substrates with the cell gap ($< 2 \mu m$ in practice) much smaller than the helical pitch, then the structure inside the cell is affected by the surface anchoring and the helical twist of the molecules is suppressed and unwound. The smectic layers are perpendicular to the substrates of the cell and the original helical axis (though unwound now) is perpendicular to the smectic layers. Under the confinement produced by the surface anchoring, there only exist two allowable directions out of the whole conic motion that the molecules can take, say, \hat{n}_1 and \hat{n}_2 , which are illustrated in Fig. 3-1-4. These two orientational states can be selected by applying an electric field across the cell with specific polarity. In this figure, when applying a downward electric field, the spontaneous polarizations tend to

align themselves with the external field and thus \hat{n}_1 is chosen by the molecules; similarly, when applying an upward electric field, \hat{n}_2 is chosen. Furthermore, if the polarizer is chosen in the direction of \hat{n}_1 with the analyzer perpendicular to it, the molecules orienting in the orientational state \hat{n}_1 induced by a downward electric field will cause no light to come out of the cell. On the other hand, when the molecules are forced to orient in the orientational state \hat{n}_2 by an upward electric field, the angle 2θ (θ is the tilt angle) between the polarization of the incident light and the LC's director gives rise to a phase retardation and thus makes the polarization of the light propagating through LC rotate, which leads to the leakage light coming out of the cell.

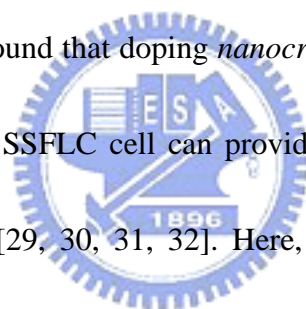


From the above discussion, we see that, for a SSFLC device, the switching between the dark state and the bright state can be easily achieved by simply altering the polarity of the applied electric field. Once either one state is turned on, it will remain on that state even after the applied electric field is removed. This is because there exists an energy barrier between these two states for the confined structure [27]. Therefore, SSFLC are bistable devices.

3.2 Experimental Study of the Dynamic Light Scattering from Pure SSFLC and Nanocrystalline–ZnO Doped SSFLC

The switching speeds in almost all LCDs (liquid crystal displays) of nowadays are mainly constrained by one of their switching mechanisms: a relaxation back to the orientation favored by the anchoring of the alignment surface when the applied electric field is removed [28]. SSFLC devices do not need to worry about this problem since the relaxation mechanism is avoided in such kinds of devices. However, in display industry, it is difficult to make quality confirmed SSFLC displays with large size because of the problem of surface irregularities [27]. Achieving a nearly perfect molecular alignment inside a SSFLC device is still an unsolved problem.

In recent years, it was found that doping *nanocrystalline-ZnO (nc-ZnO)* into the ferroelectric LC filled in the SSFLC cell can provide some degrees of freedom for tailoring material properties [29, 30, 31, 32]. Here, we shall try to probe into the validity of this viewpoint.



3.2.1 Experimental Setup

We made two kinds of SSFLC cells: with and without nc-ZnO doped. The ferroelectric LC material used in this experiment was FELIX-017/100 manufactured by *Clariant Japan*. After rubbing the alignment layer (polyimide *RN1182* manufactured by *Nissan Chemical Ltd.*) coated on the *Indium Tin Oxide (ITO)* substrates, the ferroelectric LC was infused into the cell made by the above

surface-treated substrates with the $2 \mu\text{m}$ cell gap. An undoped SSFLC cell was then obtained. On the other hand, ZnO nanocrystals with 3.4 nm average diameter were prepared for being doped into the ferroelectric LC to obtain a nc-ZnO-doped SSFLC cell in the doping level of around 1 wt %.

The experimental setup was nearly the same as that adopted in the measurement of nematic cells in Fig. 2-4-1, but a small change was introduced. In a smectic phase LC, the tilt angle subtended by the LC molecules and the layer normal is sensitive to the ambient temperature [26]. Therefore, to suppress the tilt angle fluctuations caused by the ambient temperature variations, we used an accurate heating stage with $\pm 0.1 \text{ }^\circ\text{C}$ precision. The smectic C phase's temperature range of the ferroelectric LC material we used is $-28 \text{ }^\circ\text{C}$ to $73 \text{ }^\circ\text{C}$, so that keeping the measuring temperature at $28 \text{ }^\circ\text{C}$ is a safe choice. The experimental scheme is given below.

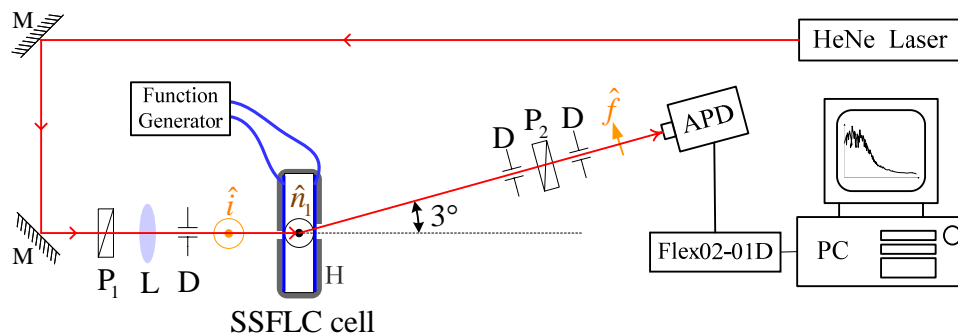


Fig. 3-2-1 The scheme is similar to that shown in Fig. 2-4-1. H represents the heating stage. Note that \hat{n}_1 is the direction in one of the two orientational states, which is shown in Fig. 3-1-4. A function generator was used to switch the SSFLC cell between two bistable states.

As shown in the figure, we still probed the dynamics parallel to both the substrates of the cell and the scattering plane for simplifying our discussion.

3.2.2 Experimental Results and Discussion

We begin the discussion by first examining the dynamical behavior of the LC molecules in the nc-ZnO-doped SSFLC cell.

Having connected the electrodes attached on the ITO of the cell to a function generator, we applied sinusoidal driving voltages ($V_{pp} = 1 \text{ V}$) to the cell with a series of frequencies, say 10 Hz , 100 Hz , 1 KHz , and 10 KHz to drive the LC molecules in the cell to fluctuate coercively. The corresponding autocorrelation functions calculated by the digital correlator Flex02-01D are shown in the following figure.

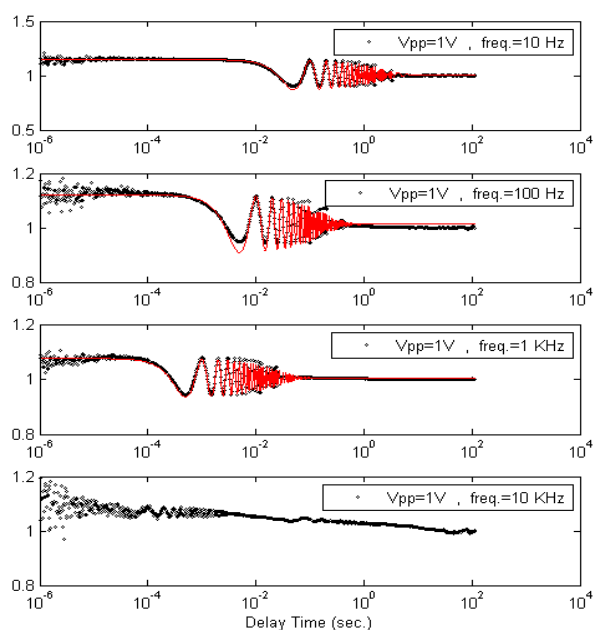


Fig. 3-2-2 The autocorrelation functions of the scattered light signals

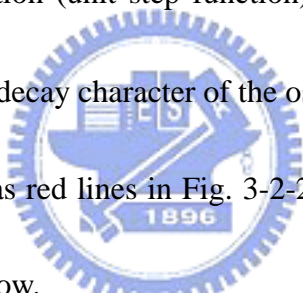
correspond to externally sinusoidal driving voltages with different driving frequencies. The small hollow circles represent the measured raw data while the red lines represent the fitting curves.

The regularly oscillating behavior of the autocorrelation functions under lower driving frequencies gives us a hint that we are supposed to use a sinusoidal function as our fitting model. The fitting model thus may take the form

$$g^{(2)}(t) = a \cdot \cos(\omega t) \cdot H(p) \cdot e^{-dt} + c, \quad (3.2.1)$$

where a is the initial fluctuation amplitude, ω is the frequency of the oscillation, $H(p)$ is the *Heaviside* function (unit step function) that stands for taking nothing until $t = p$, e^{-dt} reflects the decay character of the oscillation, and c is a constant.

The fitting curves are shown as red lines in Fig. 3-2-2 and seem quite matching. The fitting results are tabulated below.



Driven Freq. / Parameter	10 Hz	100 Hz	1 KHz
a	0.1394	0.1074	0.07044
ω	62.82	628.2	6282
p	0.01	0.001	0.0001
d	0.4536	5.496	37.16
c	1.006	1.013	1.005

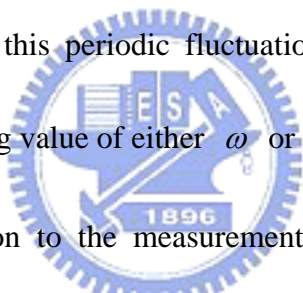
Table 3-2-1 The fitting results of Fig. 3-2-2. Note that the parameters ω and p are correlated.

The fitting results worth noting are the parameters ω and p . The unit of ω is radian per second. When it is transformed into Hz , we find that the fitting values of ω are completely equal to the driving frequencies of the applied sinusoidal driving voltages. This observation strongly implies that (1) the autocorrelation function is sensitive to the dynamics under measure, and it provides the equivalent dynamical information existing in the dynamics; (2) the motion of the LC molecules is indeed modulated by the external driving voltage coercively and coherently or else the conclusion (1) will collapse; (3) the LC molecular coherent motion is switched between the two bistable states of the nc-ZnO-doped SSFLC cell with the driving frequency suggested by (2). The fourth case in Fig. 3-2-2 can not be fitted well because the LC molecules can not keep up with such a high frequency voltage modulation any more in such a high viscous environment, and the coherent behavior with the driving frequency mentioned in the conclusion (2) was not be observed any more.

Besides ω , the fitting parameter p also could provide us with something useful. If we take a closer look into Fig. 3-2-2, we could find that the initial positions in which the function profile begins to oscillate are all different under different driving frequencies. This observation suggests that p and the driving frequency may

be correlated with each other, which leads to an assumption that p and ω are correlated with each other since ω and the driving frequency are coherent, which was confirmed by the above conclusion (2). From Table 3-2-1, the fitting results give solid evidence that p and ω are absolutely correlated with each other because of the existence of the relationship $\omega \cdot p = \text{constant}$.

Having come this far, we have obtained an informative conclusion: once we find that there exists an oscillation in the measured autocorrelation function, there must be certain kind of periodic fluctuation existing in our probing region, and even further, we can understand how fast this periodic fluctuation is oscillating, which can be simply deduced from the fitting value of either ω or p .



Let us turn our attention to the measurements of the SSFLC cells without applying any external field on them. In these measurements, unlike any before, we adopted a strategy of long time measuring. It is necessary to do so because we have no idea about what kind(s) of fluctuation(s) we shall see and how many fluctuation modes there will be in the ferroelectric LC cell with much more complicated molecular motions than those in the nematics. The knowledge background of subsection 1.3.3 has told us to adopt a measuring time over 10,000 characteristic decay time of the autocorrelation function to attain a statistical uncertainty of 1 % [11]. Compared with the fluctuation mode that corresponds to the longest characteristic

decay time, if the measuring time is not long enough, we may lose the accuracy of the dynamical information about this fluctuation mode to any extent, even lose it completely.

The measuring times we adopted in the measurements of the cases with no external field applied were all kept at 7,200 seconds. The results of the measured autocorrelation functions together with their fitting curves and their corresponding intensity (photocounts per second) traces are shown below.

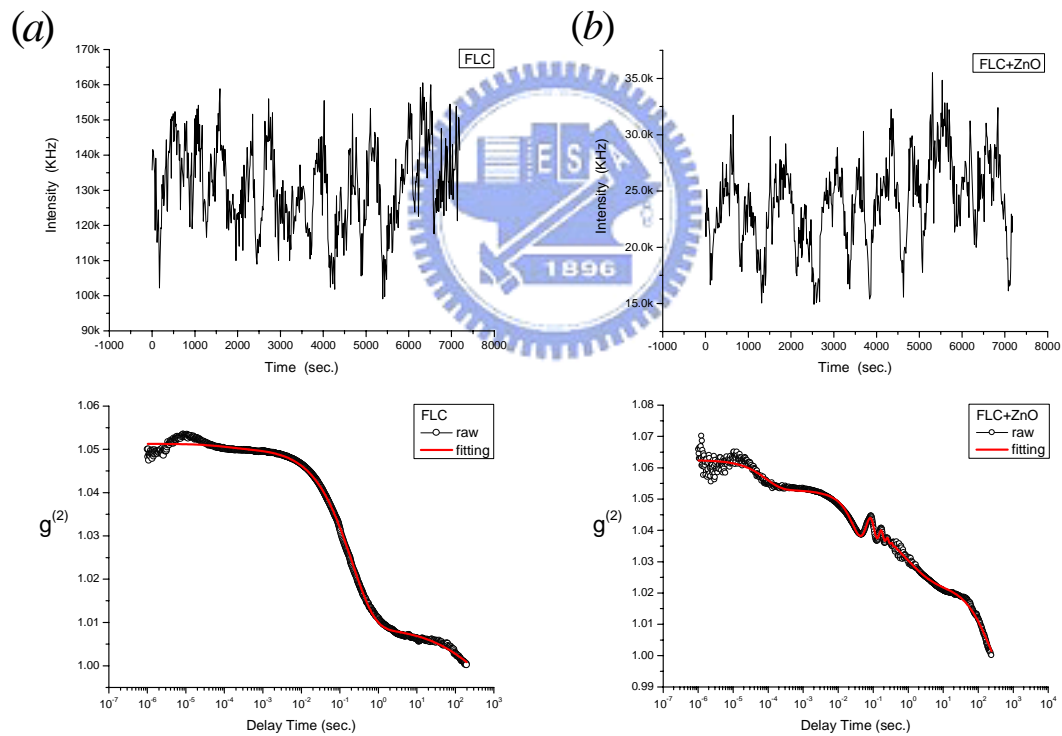


Fig. 3-2-3 (a) The top figure shows the intensity trace collected in duration of 7,200 seconds for the undoped SSFLC cell while the bottom shows the corresponding autocorrelation function (hollow circle line) and its fitting curve (red line); (b) the case for the nc-ZnO-doped SSFLC cell. Note that in both intensity traces in (a) and (b), they exhibit not only global fluctuation but also local fluctuation.

The difference deserves to be mentioned in Fig. 3-2-3 is the small oscillating ripples existing in the middle region of the autocorrelation function for nc-ZnO-doped SSFLC cell, whereas ripples do not appear for the undoped case. This obliges us to adopt different fitting models for them, which gives

$$g^{(2)}(t) = A + B \cdot e^{-(t/\tau_1)^{s_1}} + C \cdot e^{-(t/\tau_2)^{s_2}} + D \cdot e^{-(t/\tau_3)^{s_3}} \quad (3.2.2)$$

for undoped SSFLC cell and

$$g^{(2)}(t) = A + B \cdot e^{-(t/\tau_1)^{s_1}} + C \cdot e^{-(t/\tau_2)^{s_2}} + D \cdot e^{-(t/\tau_3)^{s_3}} + E \cdot \cos(\omega t) \cdot H(p) \cdot e^{-dt} \quad (3.2.3)$$

for nc-ZnO-doped SSFLC cell.

In measuring the size of *Brownian* particle in chapter 1 and the anchoring strength of nematic LC cell in chapter 2, we always applied single stretched exponential function $g^{(2)}(t) = A + B \exp\left[-(t/\tau)^s\right]$ to fit the measured raw data since the dynamical behaviors that were measured were all close to a single fluctuation mode (in *Brownian* motion case, it is translational motion; in nematic LC molecular fluctuation case, it is twist fluctuation) and a single relaxation time was thus expected. However, the situation in SSFLC seems much more complicated. In addition to the molecular conic motion that exists in the ferroelectric LC material, the restriction caused by surface constrains the LC molecular motion in switching between the two bistable states, and this may contribute a fluctuation mode. Furthermore, the existence of nc-ZnO affects some physical properties of the ferroelectric LC material [30, 31,

32], which may also contribute a different fluctuation mode. Hence, a model that describes only one single relaxation dynamics is no longer appropriate for describing the dynamics in SSFLC.

The measured raw autocorrelation function profile of the undoped SSFLC cell shown in Fig. 3-2-3 (a) gives us a hint that we can try a triple stretched exponential function of the form shown in Eq. (3.2.2) owing to the three steps appearing in its profile. The fitting results are tabulated below.

Cell Parameter	nc-ZnO-doped	undoped (a)	undoped (b)
<i>A</i>	0.9917	0.9917	0.9896
<i>B</i>	0.009248	0.0008995	NA
<i>C</i>	0.02395	0.04127	0.04199
<i>D</i>	0.03119	0.0174	0.01934
<i>E</i>	0.006359	NA	NA
s_1	1	1	NA
s_2	0.5624	0.7454	0.7155
s_3	1	0.5181	0.5208
τ_1	8.782e-005	1.168e-004	NA
τ_2	0.7885	0.2077	0.2058
τ_3	206.7	459.9	643.8
ω	73.05	NA	NA
<i>p</i>	0.01	NA	NA
<i>d</i>	8.699	NA	NA

Table 3-2-2 The fitting results of the two autocorrelation functions in Fig. 3-2-3. Here, “undoped (a)” represents the fitting results by using the fitting model Eq. (3.2.2); “undoped (b)” represents the fitting results by using a double stretched exponential function $g^{(2)}(t) = A + C \cdot e^{-(t/\tau_2)^{\alpha_2}} + D \cdot e^{-(t/\tau_3)^{\alpha_3}}$.

Note that adopting triple stretched exponential function means that we believe there may exist three exponentially decaying dynamics inside the probing region, and we mathematically combine these three exponentially decaying dynamics by simply adding up their corresponding stretched exponential functions by virtue of the linearity property of the correlation operation.

Let us try to explain what we really got from these measurements. As we have known that a ferroelectric LC molecule is in a constant conic motion, a spontaneous polarization accompanying it also rotates. However, the spontaneous polarization is induced from the unbalance of the spatial charge distribution inside the molecule. This internal unbalance is unnecessarily correlated to the ensemble behavior of the molecule. For this reason, the uncorrelation in between contributes excess degrees of freedom to the fluctuations in the ferroelectric LC material, just like that shown in Fig. 3-2-4.

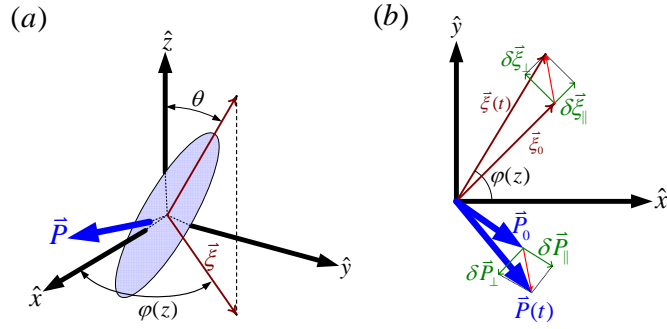


Fig. 3-2-4 In SmC^* , **(a)** $\vec{\zeta}$ is the in-plane projection of the molecular tilt and \vec{P} is the spontaneous electric polarization on a plane parallel to $\hat{x}-\hat{y}$ plane. **(b)** the small fluctuations of the tilt and the polarization [15].

Now that both the tilt part and the polarization part contribute to the ensemble fluctuations as well, it is reasonable for us to treat them as different fluctuation modes.

The parallel fluctuating component ($\delta\vec{\zeta}_{\parallel}$ and $\delta\vec{P}_{\parallel}$) thus corresponds to the *amplitude excitations* while the perpendicular fluctuating component ($\delta\vec{\zeta}_{\perp}$ and $\delta\vec{P}_{\perp}$)

corresponds to the *phase excitations* [15]. It is these two excitations that contribute to the two relaxation times τ_2 and τ_3 in Table 3-2-2. Moreover, since our experiment

was conducted at almost constant ambient temperature (with $\pm 0.1^\circ\text{C}$ precision), the fluctuation in tilt angle was supposed to be suppressed, which leads to the

difficulty of the existence of the amplitude excitations. Therefore, τ_2 was supposed to be relatively small, and this conjecture is strongly confirmed by the fitting results

shown in Table 3-2-2. In other words, we reach the point that in the ferroelectric LC the phase excitations are more popular than the amplitude excitations given that the

ambient temperature is kept constant stably. So far, we have explained the physical meaning of τ_2 and τ_3 , and the discussion seems quite reasonable. What about τ_1 ?

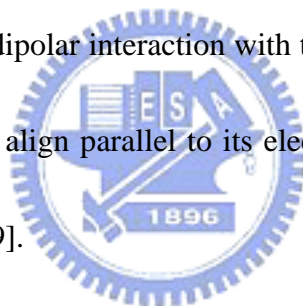
In our viewpoint, τ_1 may possibly come from the correlation of the noises that exist in our measuring system, especially those dependent of frequency, the so-call $1/f^\alpha$ noise. These kinds of noises have the “pink” character, that is, their power spectral density decays with their frequencies. According to the *Wiener-Khinchin* theorem, it is this spectrum decay with frequency that produces an equivalent correlation time.

Generally speaking, the correlation time of $1/f^\alpha$ noise is not easy to be observed when it is mixed into a relatively strong signal, but why can we extract this information? This is possibly because (1) the measuring time (7,200 seconds) was long enough (compared with the measuring time in the measurements of nematic cells) for observing it; (2) the mixing signal did not have strong correlation itself (compared with the observed strong correlation in the measurements of nematic cells), as you can see in the comparison between Fig. 3-2-3 and Fig. 1-3-6 (b) .

A final question about the fitting relaxation times may arise: how can we determine which one among τ_1 , τ_2 , and τ_3 is the minor effect coming from the $1/f^\alpha$ noise that exists in the system? To answer this question, we made a simple test as follows: using a double stretched exponential function as our fitting model to fit the raw data measured from the undoped cell. The fitting result is shown in the third

column of Table 3-2-2. Now, we can easily tell which one is the minor term coming from noise and which ones are the dominant terms coming from the two excitation modes (amplitude and phase).

Last but not least, let us examine the difference between the autocorrelation functions measured from the undoped SSFLC cell and the nc-ZnO-doped SSFLC cell. With nc-ZnO doped, the improved molecular alignment quality is expected and was really achieved in our lab. This mainly originates from the dipole-dipole interaction between the nc-ZnO and the $C=O$ groups of the surrounding ferroelectric LC. Each ZnO quantum dot provides a dipolar interaction with the surrounding ferroelectric LC molecules and forces them to align parallel to its electric polarization resulting from the internal dipole moment [29].



Note that in section 3.1, we have understood that the smectic phase has more ordered spatial arrangement of the molecules than nematic phase does, which is revealed by a fact that the smectic phase has somewhat positional order while the nematic does not. This fact strongly hints that the dynamical behavior in the smectic phase structure is supposed to be closer to that in the solid crystal structure than that in the nematic phase structure. But unlike the underdamped dynamics of the phonons in the solid crystal, molecular fluctuations in the ferroelectric LC are still overdamped, as proved in the autocorrelation function measured from the undoped SSFLC cell shown in Fig.

3-2-3 (a). However, something really interesting happened right after doping nc-ZnO into the pure ferroelectric LC cell. In Fig. 3-2-2, the LC molecules driven by the external electric field switched between the two bistable states regularly, which leads to an periodically oscillating autocorrelation function; in Fig. 3-2-3 (b), the autocorrelation function exhibits the similar oscillating part to that in Fig. 3-2-2 without any externally applied electric field. This observation strongly implies that the fluctuations in the ferroelectric LC experience a dynamical change from completely overdamped to partially overdamped and partially underdamped after doped with nc-ZnO. We attribute this underdamped component of the whole fluctuations to the better spatial molecular arrangement coming from the intrinsically positional order and the doping-induced better orientational order. It is this doping-induced effect that makes this smectic phase LC in the cell be much closer to solid crystal, and makes the molecules in the cell encounter less resistance for oscillating underdampingly. The nc-ZnO helps the molecules in the cell overcome the energy barrier put up by the surface anchoring successfully and switch between the two bistable states freely. This free switching between the two bistable states contributes another fluctuation mode to the system. However, instead of overdamped, it is a periodically underdamped mode. Furthermore, the fitting result in Table 3-2-2 also tell us that the frequency of this underdamped oscillation is 73.05 rad/sec. , which approximately equals 11.63 Hz.



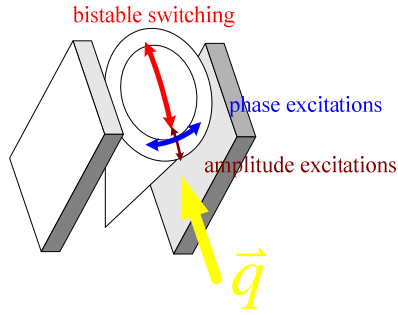


Fig. 3-2-5 The three fluctuation modes observed in the measurement. \vec{q} represents the scattering vector.

The doping level we used in the nc-ZnO-doped SSFLC cell was around 1 wt%, this leads to an estimation of $n_{FLC} \approx 15000$ ferroelectric LC molecules surrounding one ZnO nanoparticle in a spherical space of $R_{max} \doteq 14 \text{ nm}$ [29]. Because of this wide gap of ratio, not all of the molecules in the cell are affected severely by the nc-ZnO, which is illustrated in the following figure.

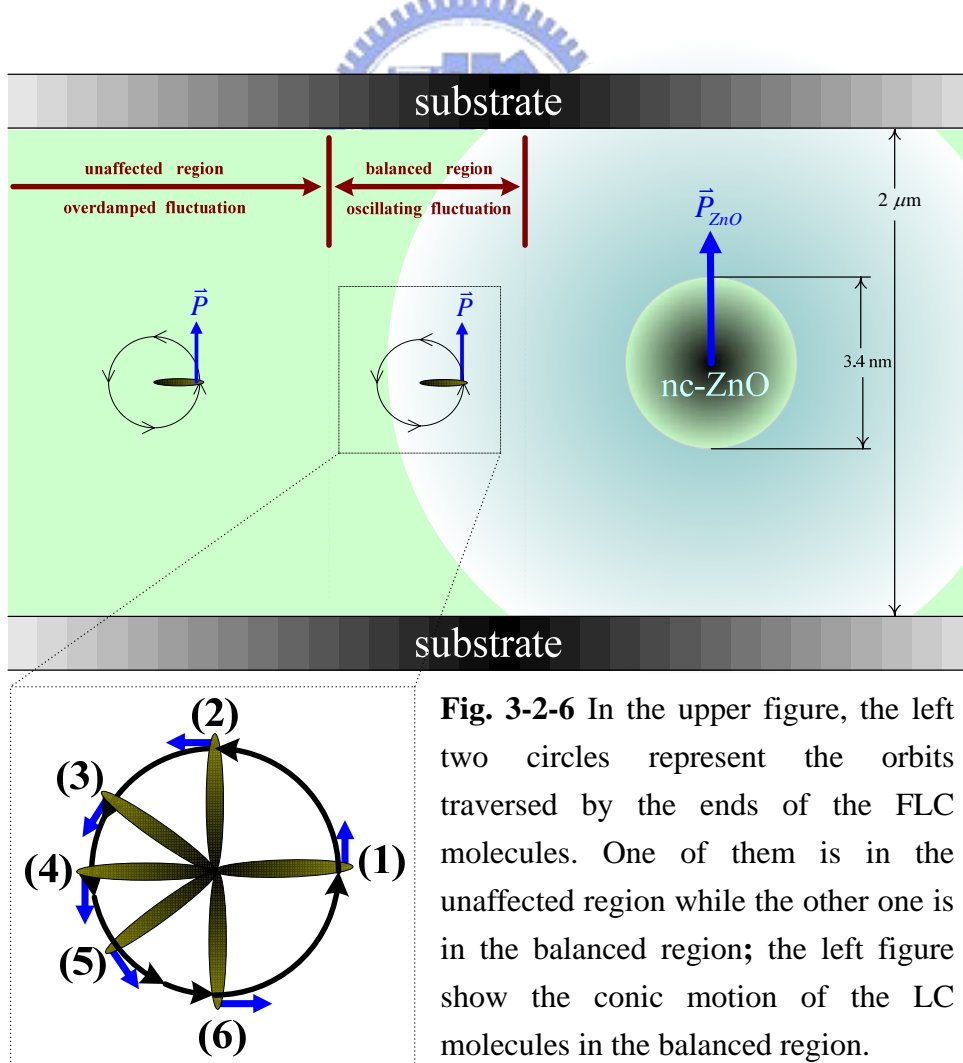
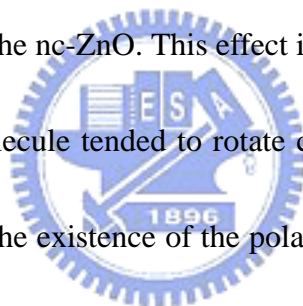


Fig. 3-2-6 In the upper figure, the left two circles represent the orbits traversed by the ends of the FLC molecules. One of them is in the unaffected region while the other one is in the balanced region; the left figure show the conic motion of the LC molecules in the balanced region.

Two mechanisms competed in affecting LC molecular dynamical behavior. As shown in this figure, the behavior of the LC molecules in the unaffected region far from the nc-ZnO was still dominated by the effect of the surface anchoring, so the bistable states were preferred in this region and the overdamped fluctuation survived; in the balanced region, the existence of the nc-ZnO, on account of highly spatial order coming from positional order and doping-induced orientational order, made the LC molecules get rid of the influence of the surface anchoring and recover their primitive conic motions. In the course of conic motion the LC molecular polarization were somewhat affected by that of the nc-ZnO. This effect is illustrated in the bottom figure of Fig. 3-2-6, when a LC molecule tended to rotate conically, say at position (4) for example, its polarization felt the existence of the polarization of the nc-ZnO so that it speeded up toward the position at which its polarization could be parallel to that of the nc-ZnO. Therefore, an accelerated pathway $(4) \rightarrow (5) \rightarrow (6) \rightarrow (1)$ was possibly set up. Likewise, a decelerated pathway $(1) \rightarrow (2) \rightarrow (3) \rightarrow (4)$ was also expected. Once a motion in such pathways happened, it can bring about a periodic motion between the two bistable states. This picture gives a direct insight into the existence of the oscillating behavior observed in the autocorrelation function measured from the nc-ZnO-doped SSFLC cell.



Chapter 4. Conclusions

To summarize, this thesis study confirmed several facts that have been well developed in some other ways, provided several intuitively physical pictures for several complex theoretical notions, and observed a dynamical phenomenon never found before. Recapitulating as follows,

- (1) The hydrodynamic diameters of the nanoparticles suspending in the solution can be determined accurately by the dynamic light scattering technique.
- (2) The theoretical derivations of the relationships between the measured correlation time and the cell's anchoring strength were achieved.
- (3) The fact that the anchoring strength of the photoalignment cell is smaller than that of the mechanical rubbing cell was confirmed.
- (4) Liquid crystal polymers do improve the surface alignment quality.
- (5) The autocorrelation functions measured from the SSFLC were observed successfully; the fitting results are in accordance with the intuitive physical models.
- (6) A transformation of fluctuation mode in the measurement of the nc-ZnO-doped SSFLC cell from completely overdamped to partially overdamped and partially underdamped was discovered.

(7) A model responsible for the explanation of the transformation in (6) was presented.



References

- [1] Kerson Huang, *Introduction to Statistical Physics*, Taylor & Francis, London, 2001.
- [2] Don S. Lemons, *An Introduction to Stochastic Process in Physics*, The Johns Hopkins University Press, Baltimore and London, 2002.
- [3] F. Reif, *Fundamentals of Statistical and Thermal Physics*, McGraw-Hill, New York, 1974.
- [4] Daniel T. Gillespie, "The Mathematics of Brownian Motion and Johnson Noise", *Am. J. Phys.*, 64, 225, March 1996.
- [5] Bruce J. Berne and Robert Pecora, *Dynamic Light Scattering: With Applications to Chemistry, Biology, and Physics*, Dover Publications, Mineola and New York, 2000.
- [6] Strahinja Stojadinovic, "Light Scattering Studies of Dynamics of Bent-Core Liquid Crystals", Kent State University, Ph.D. Dissertation, May 2005.
- [7] Benjamin Chu, *Laser Light Scattering: Basic Principles and Practice*, Academic Press, Boston, 1991.
- [8] Noel A. Clark, Joseph H. Lunacek, and George B. Benedek, "A Study of Brownian Motion Using Light Scattering", *Am. J. Phys.*, 38, 575, May 1970.
- [9] PHY4803L-Advanced Physics Laboratory, "Dynamic Light Scattering: Experiment DLS", University of Florida - Department of Physics, May 29, 2007.
- [10] Christer Svanberg and Rikard Bergman, "Photon Correlation Spectroscopy", Chalmers University of Technology, September 2005.
- [11] Luca Cipelletti and D. A. Weitz, "Ultralow-Angle Dynamic Light Scattering with A Charge Coupled Device Camera Based Multispeckle, Multitau Correlator", *Rev. Sci. Instrum.*, 70, 3214, August 1999.
- [12] Peter J. Collings, *Liquid Crystals: Nature's Delicate Phase of Matter*, Princeton University Press, New Jersey, 2002.
- [13] Iam-Choon Khoo, *Liquid Crystals: Physical Properties and Nonlinear Optical Phenomena*, John Wiley & Sons, New York, 1995.
- [14] P.G. de Gennes and J. Prost, *The Physics of Liquid Crystals*, Oxford University Press, Oxford, 1993.
- [15] I. Musevic, R. Blinc, B. Zeks, *The Physics of Ferroelectric and Antiferroelectric Liquid Crystals*, World Scientific, London, 2000.
- [16] J. R. Kelly and P. Palffy - Muhoray, "Normal Modes of Director Fluctuations in a Nematic Droplet", *Phys. Rev. E*, 55, 4378, April 1997.

- [17] S. Stallinga, M. M. Wittebrood, D. H. Luijendijk, and Th. Rasing, "*Theory of Light Scattering By Thin Nematic Liquid Crystal Films*", Phys. Rev. E, 53, 6085, June 1996.
- [18] Orsay Liquid Crystal Group, "*Dynamics of Fluctuations in Nematic Liquid Crystals*", J. Chem. Phys., 51, 816, 15 July 1969.
- [19] Mojca Vilfan, I. Drevensek Olenik, A. Mertelj, and M. Copic, "*Aging of Surface Anchoring and Surface Viscosity of a Nematic Liquid Crystal on Photoalignment Poly-(vinyl-cinnamate)*", Phys. Rev. E, 63, 061709, 2001.
- [20] Mojca Vilfan, Alenka Mertelj, and Martin Copic, "*Dynamic Light Scattering Measurements of Azimuthal and Zenithal Anchoring of Nematic Liquid Crystals*", Phys. Rev. E, 65, 041712, 2002.
- [21] Mojca Vilfan and Martin Copic, "*Azimuthal and Zenithal Anchoring of Nematic Liquid Crystals*", Phys. Rev. E, 68, 031704, 2003.
- [22] A. P. Davey, R. G. Howard, W. J. Blau, and H. J. Byrne, "*Polarized Photoluminescence and Measurement of Degree of Order in Mixed Oriented Polymer Liquid Crystal Films*", Intern. J. Polymeric Mater., 44, 241, 1999.
- [23] H. Kihara, T. Miura, and R. Kishi, "*Morphological Studies of LC Polymer Networks Prepared by Photopolymerization of (LC Monomer/LC) Blends*", Polymer, 43, 4523, 2002.
- [24] Heiko Thiem, Peter Stroehriegl, Maxim Shkunov, and Iain McCulloch, "*Photopolymerization of Reactive Mesogens*", Macromol. Chem. Phys., 206, 2153, 2005.
- [25] A. V. Zakharov, "*Rotational Viscosity in a Nematic Liquid Crystal: A Theoretical Treatment and Molecular Dynamics Simulation*", Phys. Rev. E, 59, 6802, June 1999.
- [26] Toralf Scharf, *Polarized Light in Liquid Crystals and Polymers*, John Wiley & Sons, New Jersey, 2007.
- [27] D. K. Yang and S. T. Wu, *Fundamentals of Liquid Crystal Devices*, John Wiley & Sons, England, 2006.
- [28] Peter J. Collings, "*Ferroelectric Liquid Crystals: The 2004 Benjamin Franklin Medal in Physics presented to Robert B. Meyer of Brandeis University*", J. Franklin Institute, 342, 599, 2005.
- [29] Jung Y. Huang, L. S. Liu, and M. C. Chen, "*Probing Molecular Binding Effect from Zinc Oxide Nanocrystal Doping in Surface-Stabilized Ferroelectric Liquid Crystal with Two-Dimensional Infrared Correlation Technique*", J. Phys. Chem. C, 112, 5410, April 10, 2008.
- [30] M. Marinelli, A. K. Ghosh, and F. Mercuri, "*Small Quartz Silica Spheres Induced Disorder in 8CB Liquid Crystals: A Thermal Study*", Phys. Rev. E, 63, 061713,

2001.

[31] Yukihide Shiraishi, et al., "*Frequency Modulation Response of a Liquid-Crystal Electro-Optic Device Doped with Nanoparticles*", Appl. Phys. Lett., 81, 2845, October 7, 2002.

[32] S. Kaur, et al., "*Enhanced Electro-Optical Properties in Gold Nanoparticles Doped Ferroelectric Liquid Crystals*", Appl. Phys. Lett., 91, 023120, July 13, 2007.

